nature communications

Article

https://doi.org/10.1038/s41467-026-71727-y

RPS19 and RPL5 haploinsufficient models reveal divergent ribosomal subunit controls of fetal hematopoiesis

Received: 11 September 2025

Accepted: 27 March 2026

Published online: 08 April 2026

Check for updates

Yuefeng Tang[1,2,15], Te Ling[3,15], Rashid Mehmood[3,15], Alexis Bertrand[1], Julien Papoin[1,2], Mushran Khan[1], Riaz Rao[1], Jianing Xu[4], Vincent Schulz[5], James Palis[6], Laurie A. Steiner[6], Betsy J. Barnes[1,2], Yong-Rui Zou[1,2], Philippe Marambaud[1,2], Robert A. J. Signer[7], Irene Roberts[8], Deena Iskander[9], Leonard I. Zon[10], Senthil Velan Bhoopalan[3], Mitchell J. Weiss[3], Jeffrey M. Lipton[1,2], Patrick G. Gallagher[11], Narla Mohandas[12], Naomi Taylor[13,16], Sébastien Durand[14,16], John Crispino[3,16] & Lionel Blanc[1,2,16]

Diamond Blackfan anemia syndrome (DBAS) is a congenital ribosomopathy caused by haploinsufficiency of ribosomal proteins (RPs), but how RP stoichiometry and activity regulates erythroid development remains enigmatic. Using in vivo models, we uncover divergent functions for the small and large ribosomal subunit proteins RPS19 and RPL5 in fetal hematopoiesis. While RPL5 haploinsufficiency causes hematopoietic stem and progenitor cell (HSPC) accumulation and prenatal lethality via p53-mediated ferroptosis of mature erythroid progenitors, RPS19 haploinsufficiency leads to HSPC depletion and impaired erythroid expansion through p53-dependent apoptosis. The latter is accompanied by translational and transcriptional dysregulation, including the upregulation of *RUNX1*, which is also observed in RPS- haploinsufficient DBAS patients. Importantly, *Runx1* deletion in RPS19-haploinsufficient mice partially rescues HSPC numbers. These findings reveal subunit-specific RP functions in controlling fetal hematopoiesis and demonstrate how imbalanced RP stoichiometry disrupts developmental programs, providing crucial mechanistic insights into DBAS pathogenesis and the basis for its clinical heterogeneity.

Dysregulation of translational control occurs in numerous contexts including cell growth and development, aging, immunity, and responses to environmental changes and may contribute to malignancy, inflammation, autoimmune disease, and other disorders[1–3]. Ribosomopathies are a group of inherited disorders associated with ribosomal protein haploinsufficiency or defects in ribosome biogenesis[4]. While all cells require ribosomes, ribosomopathies often demonstrate tissue-specific defects, sometimes with increased cancer

[1]Northwell, 2000 Marcus Ave, Suite 300, New Hyde Park, NY, USA. [2]Zucker School of Medicine at Hofstra/Northwell, Hempstead, NY, USA. [3]St. Jude Children's Research Hospital, Memphis, TN, USA. [4]Fudan University, Shanghai, China. [5]Yale University, New Haven, CT, USA. [6]University of Rochester Medical Center, Rochester, NY, USA. [7]University of California San Diego, La Jolla, CA, USA. [8]Weatherall Institute of Molecular Medicine, University of Oxford, Oxford, UK. [9]Department of Immunology and Inflammation, Imperial College, London, W12 0HS, and St Mary's Hospital, London, UK. [10]Boston Children's Hospital, Boston, MA, US. [11]Nationwide Children's Hospital, Columbus, OH, USA. [12]Lindsey F. Kimball Research Institute, New York Blood Center, New York, NY, USA. [13]NCI, Pediatric Oncology Branch, Bethesda, MD, USA. [14]Centre de Recherche en Cancérologie de Lyon (CRCL), Université Claude Bernard Lyon 1, INSERM U1052, CNRS UMR5286, Centre Léon Bérard, Lyon, France. [15]These authors contributed equally: Yuefeng Tang, Te Ling, Rashid Mehmood. [16]These authors jointly supervised this work: Naomi Taylor, Sébastien Durand, John Crispino, Lionel Blanc. e-mail: Lblanc@northwell.edu

susceptibility[5]. Inherited ribosomopathies with hematologic features include Diamond Blackfan anemia syndrome (DBAS), Schwachman Diamond syndrome (SDS), and X-linked dyskeratosis congenita, among others[6]. DBAS, the archetype of ribosomopathy[4], is a congenital bone marrow failure syndrome commonly associated with mutations or deletions of ribosomal genes, leading to ribosomal haploinsufficiency, resulting in nucleolar stress and p53 activation[7]. While p53 inhibition is known to ameliorate anemia in DBAS, the precise underlying mechanisms remain poorly understood[8].

Ribosomopathies remain challenging to study within the hematopoietic system, and few animal models have successfully recapitulated the diverse clinical features of the diseases[9,10]. In the context of DBAS, previous attempts to generate animal models with germline deletions of ribosomal proteins[11,12] revealed that complete knockout led to pre-implantation embryonic lethality, whereas heterozygous RP deletion resulted in minimal or no noticeable phenotype. Conditional knockout mouse models, under constitutive or inducible promoters, have been generated and display some hematopoietic phenotypes upon RP deletion[9,13]. However, these models do not present reduced reticulocyte counts likely due to compensatory splenic stress erythropoiesis, a process that does not appear to occur in humans[14]. Clinically, DBAS usually manifests soon after birth and is characterized by macrocytosis, reticulocytopenia and a scarcity of erythroid precursors in the bone marrow[15]. The presence of other hematopoietic lineage defects in certain patients suggests a broader underlying defect in hematopoietic stem and/or progenitor cells (HSPCs)[16,17]. However, these aspects remain understudied, and it is unclear whether they are a universal consequence of RP mutations or whether there are differences specific to mutations in large versus small subunits. Thus, DBAS presents a unique framework to uncover novel pathways by which ribosomal subunits regulate hematopoiesis.

To investigate how specific RP subunits contribute to this process, we generated in vivo mouse models of RPS19 and RPL5 haploinsufficiency and performed mechanistic studies during fetal development. Our findings reveal distinct, subunit-specific roles for RPS19 and RPL5 in fetal hematopoiesis, uncovering specific roles of these RPs in fetal hematopoiesis. These results demonstrate new physiological and divergent functions for ribosomal proteins and provide insights into how disrupted RP stoichiometry alters developmental hematopoiesis and contributes to disease pathogenesis.

Results

Hematopoietic heterozygous deletion of *Rps19* or *Rpl5* phenocopies DBAS

To gain insights into the role of RPs during hematopoiesis, we generated conditional mouse models using CRISPR-Cas9 editing to delete specific regions of the *Rps19* and *Rpl5* genes—two of the most frequently mutated RP in DBAS (Supplementary Fig. 1a, b). The use of the *Vav-Cre* promoter restricts the Cre activity to the hematopoietic system beginning at midgestation[18,19]. We noticed that, while there was no *in utero* loss of $Rps19^{lox/+}$ fetuses, pups did not reach weaning age (Fig. 1a). Survival analyses demonstrated that $Vav\text{-}Cre^{+}; Rps19^{lox/+}$ mice (hereafter referred to as $Rps19^{lox/+}$) began dying after birth and were all dead by postnatal day 10 (P10) (Fig. 1b). These mice were paler and smaller (Fig. 1c) and complete blood counts revealed pancytopenia suggestive of bone marrow failure (Fig. 1d). Analysis of red cell indices revealed a significant increase in their mean cell volume (MCV), which was not due to reticulocytosis, since the reticulocyte count was dramatically reduced, in contrast to previous models (Fig. 1d).

In mice, the spleen assumes a hematopoietic function at birth and during periods of hematopoietic stress, especially during erythroid stress[14]. Notably, the spleens of $Rps19^{lox/+}$ mice were atrophic (Fig. 1e, black arrows). Further, gross and histological analyses of hematopoietic tissues[20] revealed a severely hypocellular bone marrow and an absence of red cell precursors in both the liver and spleen of $Rps19^{lox/+}$ at P6 (Fig. 1e, f).

In contrast, heterozygous deletion of *Rpl5* under the *Vav* promoter led to perinatal lethality (Fig. 1g). $Vav\text{-}Cre^{+}; Rpl5^{lox/+}$ embryos (hereafter referred to as $Rpl5^{lox/+}$) were detected at Mendelian ratios at E17.5 but none survived to birth, suggesting that *Rpl5* heterozygosity results in late- gestation lethality (Fig. 1g). Together, these models provide a valuable resource to address critical, mechanistic, questions related to the role of RP in fetal hematopoiesis.

Fetal erythropoiesis disruption in RPS19/RPL5 haploinsufficiency

To understand the striking phenotypic differences observed in our *Rps19* and *Rpl5* DBAS models, we studied hematopoiesis in wild-type (WT) and heterozygous mouse embryos. Immunoblot analyses confirmed that heterozygous deletion of *Rps19* and *Rpl5* resulted in an ~50% reduction in their respective protein levels in fetal liver cells (Supplementary Fig. 2a). $Rps19^{lox/+}$ embryos at E13.5 and E17.5 were slightly paler compared to their WT littermates. This was associated with a ~ 50% decrease in both total and red cell progenitor ($Ter119^{+}$) cell numbers, underpinning anemia (Fig. 2a, b). Flow cytometry assays—using CD71 and Ter119 markers to quantify distinct stages of fetal erythropoiesis (Fig. 2c)[21]—revealed an accumulation of early erythroid progenitors (S0) at E13.5 (Fig. 2d, and Supplementary Fig. 2b, c). Conversely, this same progenitor population was significantly reduced at E17.5 (Fig. 2e, Supplementary Fig. 2d). Erythropoiesis was not completely blocked, however, as red cells (S5) were produced, albeit in reduced numbers (Supplementary Fig. 2b–d). Together, these results strongly suggest that RPS19 haploinsufficiency causes anemia during fetal life by impairing erythroid progenitor development.

In contrast, $Rpl5^{lox/+}$ embryos revealed a more severe phenotype. At E13.5 the embryos were noticeably paler than WT littermates and by E17.5, the embryos were smaller and severely anemic (Fig. 2f). Similar to $Rps19^{lox/+}$, $Rpl5^{lox/+}$ embryos displayed a 2-fold reduction in total fetal liver cellularity, with a similar reduction in $Ter119^{+}$ cells (Fig. 2g). At E13.5, a decrease in the S3 erythroid progenitor population was also observed in $Rpl5^{lox/+}$ embryos (Fig. 2h, and Supplementary Fig. 2e, f). Notably though, the impact of *Rpl5* and *Rpl5* haploinsufficiency on more primitive $Ter119^{-}$ progenitors (S0) differed markedly by day E17.5. While this S0 population was significantly decreased in $Rps19^{lox/+}$ embryos, it was dramatically increased in $Rpl5^{lox/+}$ embryos (Fig. 2h, i, and Supplementary Fig. 2f, g). Indeed, in $Rpl5^{lox/+}$ embryos, the effects were largely restricted to $Ter119^{+}$ S3 erythroid cells. Taken together, these data demonstrate that while both RPS19 and RPL5 haploinsufficiency lead to decreased red blood cell production during fetal erythropoiesis, the underlying mechanisms leading to erythroid failure differ. Specifically, the loss of early erythroid progenitors by E17.5 is unique to $Rps19^{lox/+}$ and not observed in $Rpl5^{lox/+}$ embryos.

RPS19/RPL5 haploinsufficiency differentially impact fetal HSPCs

Based on our characterization of these mouse models, and the observation that $Rps19^{lox/+}$ mice present at birth with pancytopenia (Fig. 1d), we hypothesized that *Rps19* and *Rpl5* haploinsufficiency leads to disparate defects on the fetal HSPC compartment. To test this hypothesis, we quantified the different HSPC populations at E13.5 and E17.5 using commonly used cell surface markers[22](Fig. 2j, k). Within the lineage-negative (Lin-) population, the LSK ($Lin^{-}Sca1^{+}c\text{-}Kit^{+}$) compartment can be divided into three HSPC subpopulations; the most primitive LT-HSC ($CD150^{+}CD48^{-}LSK$) can produce all hematopoietic cell types following transplantation for >16 weeks whereas ST-HSC ($CD150^{-}CD48^{-}LSK$) regenerate hematopoietic cells only transiently and MPP ($CD48^{+}LSK$) represent lineage-biased subsets[23]. While at E13.5, significantly higher levels of LT-HSC and ST-HSC were detected in both $Rps19^{lox/+}$ and $Rpl5^{lox/+}$ embryos, relative to WT embryos (Fig. 2l, m), by E17.5, there was a dramatic loss of LT-HSC, and ST-HSC in $Rps19^{lox/+}$

https://doi.org/10.1038/s41467-026-71727-y

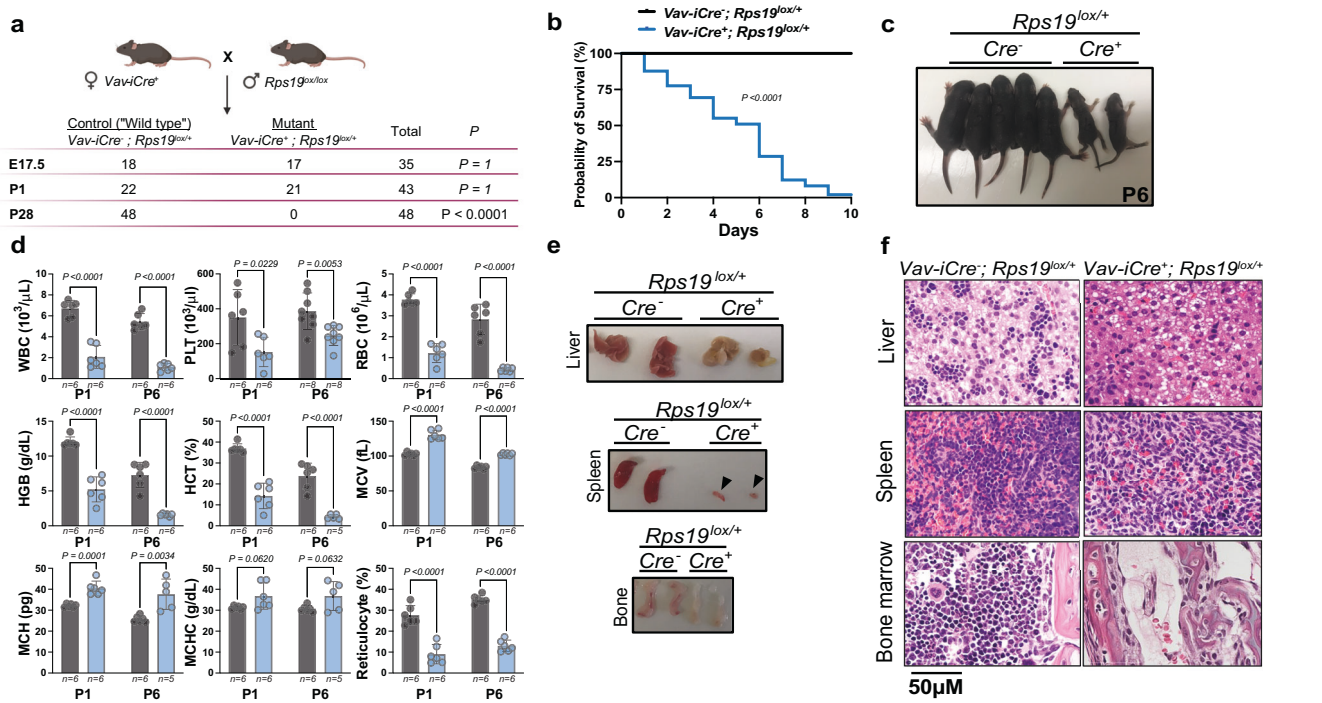

Fig. 1 | Deletion of one copy of *Rps19* or *Rpl5* leads to severe hematopoietic defects at birth. a Genotype counts from *Rps19*$^{lox/+}$ intercrossing. Statistical analysis was performed using unpaired t-test with Bonferroni correction for multiple comparisons. Created in BioRender. Blanc, L. (https://BioRender.com/ql4svuv). **b** Survival curves from *Rps19*$^{lox/+}$ mice. Statistical analysis was performed using Mantel-Cox log rank test. **c** Photos of control (*Cre*$^{-}$) and mutant (*Cre*$^{+}$) *Rps19*$^{lox/+}$ 6 days after birth (P6). **d** Complete blood counts at P1 and P6. Upper panel: white blood cells (WBC), platelets (PLT), red blood cells (RBC). Middle panel: hemoglobin (HGB), hematocrit (HCT), mean corpuscular volume (MCV). Lower panel: mean corpuscular hemoglobin (MCH), mean corpuscular hemoglobin concentration (MCHC), reticulocytes. The number of biological replicates (*n*) is indicated in italics under each histogram. Statistical analysis was performed using unpaired t-test with Holm-Šídák correction. **e** Images of the liver, spleen and bone marrow at P6 in control and mutant *Rps19*$^{lox/+}$. The arrow denotes the mutant spleen. **f** Light microscopy images (hematoxylin and eosin) highlighting the architecture and cellular composition of the same hematopoietic organs in control and mutant *Rps19*$^{lox/+}$ mice at P6. Images are representative of 3 independent experiments. **g** Genotype counts from *Rpl5*$^{lox/+}$ mice. Created in BioRender. Blanc, L. (https://BioRender.com/ql4svuv). Statistical analysis was performed using unpaired t-test with Bonferroni correction for multiple comparisons. The number of biological replicates (*n*) is indicated in italics under each histogram. All data are presented as mean ± standard deviation. Source data are presented in Source Data file.

embryos to almost undetectable levels (Fig. 2l). In marked contrast, LT-HSC, and ST-HSC were increased by 4-6-fold in *Rpl5*$^{lox/+}$ embryos by E17.5, relative to their WT counterparts (Fig. 2m). These data indicate that *Rps19* but not *Rpl5* haploinsufficiency is deleterious to HSPCs. Furthermore, these data suggest that *Rpl5*$^{lox/+}$ HSPCs expand, likely to try and compensate for the severe erythropoietic defects.

However, despite increased numbers, these progenitors were markedly defective in their ability to generate colony forming units (CFU) in vitro; the most severe defect was detected in the potential of these progenitors to form erythroid (BFU-E) as compared to myeloid (CFU-GM) colonies (Fig. 2n, **o**). Together, these results demonstrate specific requirements for RPS19 and RPL5 in shaping the HSC and progenitor compartments during fetal development.

Increased translation in fetal HSPCs from *Rps19*$^{+/-}$ and *Rpl5*$^{+/-}$ mice

The disparate roles of *Rps19* and *Rpl5* in supporting HSPC maintenance −with a loss of progenitors in the former and an accumulation of functionally abnormal progenitors in the latter, raised the question of whether this might reflect differential effects of small versus large ribosomal subunit deficiency on RP stoichiometry and protein synthesis. As RPs assemble into functional ribosomal subunits to sustain mRNA translation, we performed polysome profiling experiments to analyze 40S and 60S abundance (Fig. 3a). Due to the limited numbers of HSPCs, we performed polysome profiling in the c-Kit^{+} HSPCs. *Rps19*$^{lox/+}$ and *Rpl5*$^{lox/+}$ progenitors revealed a decrease in the 40S and 60S fractions, respectively (Fig. 3a, b). Despite this defect in ribosome biogenesis, it was surprising to detect an increase in the ratio of polysome/80S in *Rps19*$^{lox/+}$ and *Rpl5*$^{lox/+}$ c-Kit^{+} HSPCs but not in Ter119^{+} erythroblasts. These data suggest a potential increased mRNA translation specifically in c-Kit^{+} progenitors (Fig. 3a, b).

We therefore directly measured global protein synthesis in E13.5 HSPCs and Ter119+ cells, as a function of o-propargyl-puromycin (OPP) incorporation[24]. Surprisingly, OPP incorporation was significantly higher in *Rps19*$^{lox/+}$ and *Rpl5*$^{lox/+}$ LSK populations compared to control littermates. Interestingly, the magnitude of the increase was significantly greater in *Rps19*$^{lox/+}$ LSK cells, as compared to *Rpl5*$^{lox/+}$ LSK cells, in comparison to their respective littermate controls (Fig. 3c).

https://doi.org/10.1038/s41467-026-71727-y

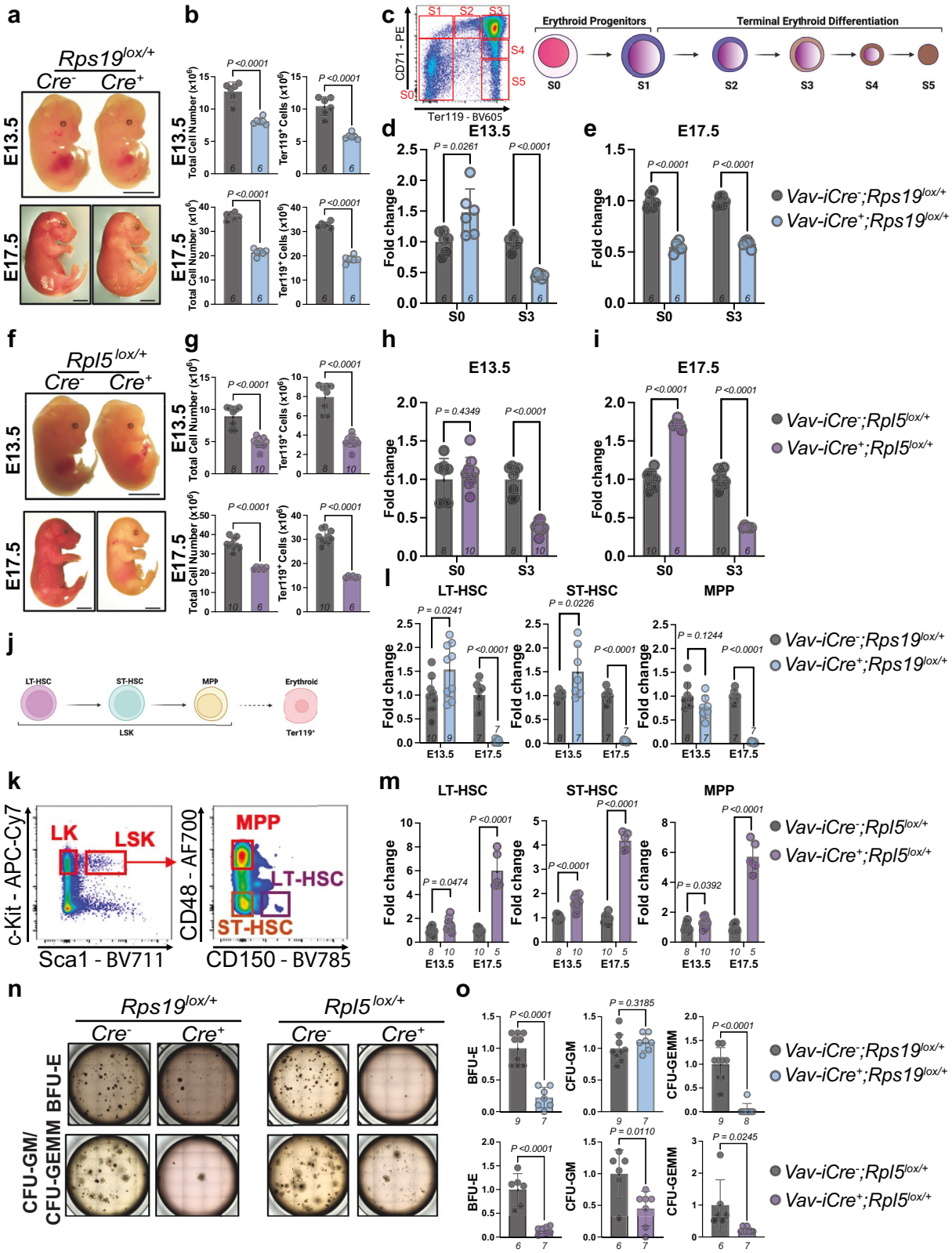

Increased protein synthesis is not well tolerated by adult HSCs and impairs their function and self-renewal. These data suggest that fetal HSCs, which have higher protein synthesis, may partially tolerate elevated protein synthesis rates in the context of *Rpl5*$^{lox/+}$ haploinsufficiency, but the magnitude of the effect in *Rps19*$^{lox/+}$ could contribute to HSC depletion. In contrast to LSK cells, OPP incorporation was significantly reduced in Ter119^{+} erythroblasts from both *Rps19*$^{lox/+}$ and *Rpl5*$^{lox/+}$ mice (Fig. 3c, and Supplementary Fig. 3a). These data indicate that HSPCs, but not erythroid cells, can compensate for the loss of ribosomes by increasing protein synthesis. This suggests that HSPCs have excess ribosome capacity, but that ribosomes are more limiting for translational activity in erythroid lineage cells.

To gain additional mechanistic insight into the compensatory increase in HSPC protein synthesis, we performed western blot

https://doi.org/10.1038/s41467-026-71727-y

Fig. 2 | Deletion of one allele of Rps19 or Rpl5 leads to divergent effects on the hematopoietic stem and progenitor cell (HSPC) compartment during fetal hematopoiesis. a Images of E13.5 (upper) and E17.5 (lower) control and *Rps19*$^{lox/+}$ embryos. **b** Fetal liver (FL) cellularity and Ter119$^+$ counts in E13.5 (upper) and E17.5 (lower) control and *Rps19*$^{lox/+}$ embryos. Statistical analysis was performed using two-tailed unpaired t-test. **c** Gating strategy to assess erythropoiesis in the FL. Created in BioRender. Blanc, L. (https://BioRender.com/i1f4n4v). **d** Quantification of cells in S0 and S3 in E13.5 control, and *Rps19*$^{lox/+}$ embryos expressed as a fold change relative to control. Statistical analysis was performed using welch t-test with Holm-Šídák correction. **e** Quantification of cells in S0 and S3 in E17.5 control, and *Rps19*$^{lox/+}$ embryos expressed as a fold change relative to control. Statistical analysis was performed using welch t-test with Holm-Šídák correction. **f** Images of E13.5 (upper) and E17.5 (lower) control and *Rpl5*$^{lox/+}$ embryos. Statistical analysis was performed using two-tailed unpaired t-test (**g**) FL cellularity and Ter119+ counts in E13.5 (upper) and E17.5 (lower) control and *Rpl5*$^{lox/+}$ embryos. Statistical analysis was performed using two-tailed unpaired t-test. **h** Quantification of cells in S0 and S3 in E13.5 control, and *Rpl5*$^{lox/+}$ embryos expressed as a fold change relative to control. Statistical analysis was performed using welch t-test with Holm-Šídák correction. **i** Quantification of cells in S0 and S3 in E17.5 control, and *Rpl5*$^{lox/+}$ embryos expressed as a fold change relative to control. Statistical analysis was performed using welch t-test with Holm-Šídák correction (**j**) Schematic representation of the HSPC populations used in the study. Created in BioRender. Blanc, L. (https://BioRender.com/i1f4n4v). **k** Gating strategy to assess early hematopoiesis in the FL. **l** Quantification of the different HSPC populations in E13.5 and E17.5 control and *Rps19*$^{lox/+}$embryos expressed as a fold change relative to control. Statistical analysis was performed using two-tailed unpaired t-test. **m** Quantification of the different HSPC populations in E13.5 and E17.5 control and *Rpl5*$^{lox/+}$embryos expressed as a fold change relative to control. Statistical analysis was performed using two-tailed unpaired t-test. **n** Representative images of colony-forming assays performed in E13.5 control, *Rps19*$^{lox/+}$ and *Rpl5*$^{lox/+}$ embryos. BFU-E: burst-forming unit-erythroid, CFU-GM: colony-forming unit- granulocyte/macrophage, CFU-GEMM:colony-forming unit-granulocyte, erythrocyte, monocyte and macrophage. **o** Quantification of colonies obtained from E13.5 control, *Rps19*$^{lox/+}$ and *Rpl5*$^{lox/+}$ embryos. Statistical analysis was performed using two-tailed unpaired t-test. The number of biological replicates (*n*) is indicated in italics under each histogram. All data are presented as mean ± standard deviation. All replicates are biologically independent. Source data are presented in Source Data file.

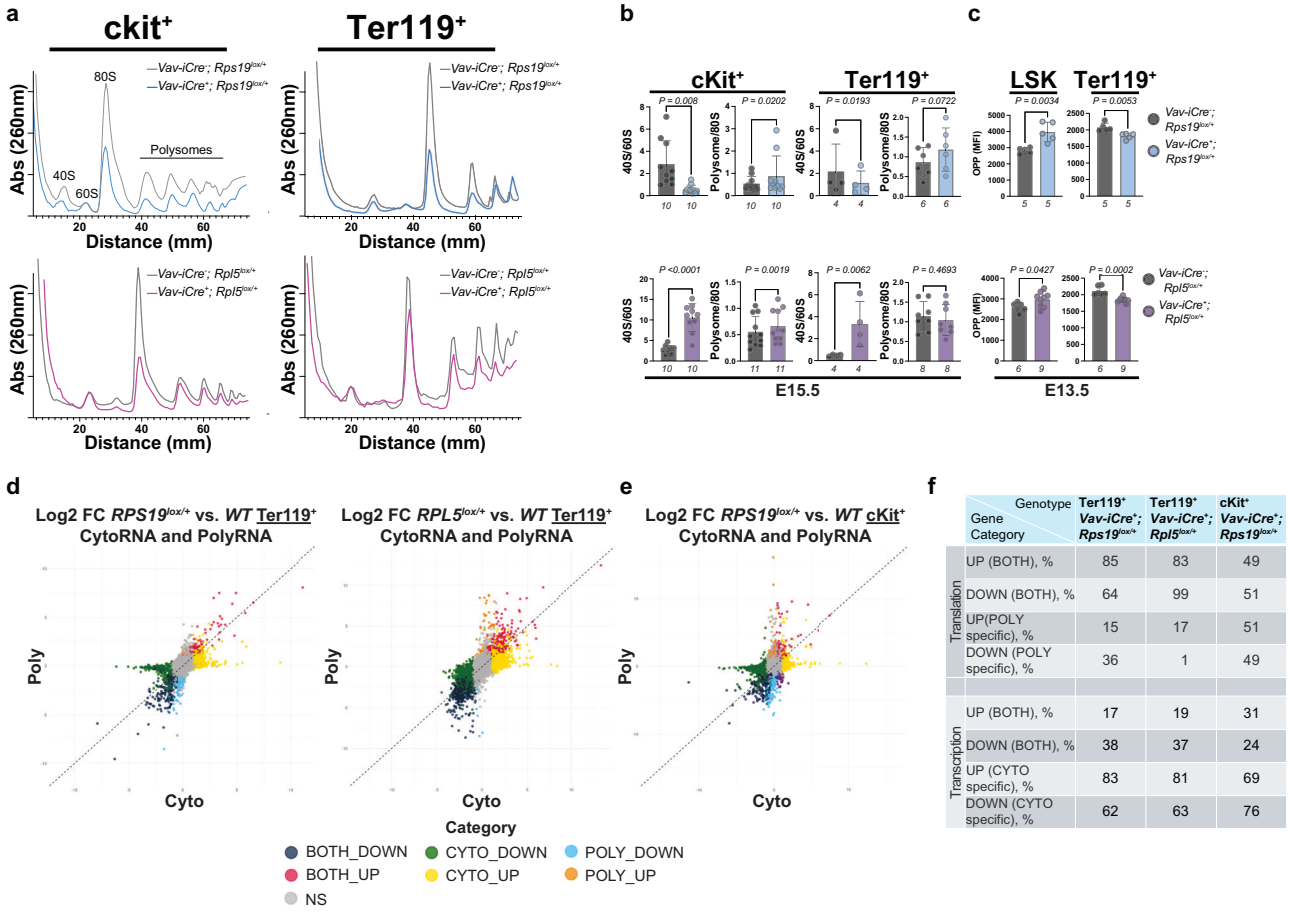

f

Gene Category \ Genotype	Ter119$^+$ *Vav-iCre$^+$; Rps19$^{lox/+}$*	Ter119$^+$ *Vav-iCre$^+$; Rpl5$^{lox/+}$*	cKit$^+$ *Vav-iCre$^+$; Rps19$^{lox/+}$*
Translation			
UP (BOTH), %	85	83	49
DOWN (BOTH), %	64	99	51
UP(POLY specific), %	15	17	51
DOWN (POLY specific), %	36	1	49
Transcription			
UP (BOTH), %	17	19	31
DOWN (BOTH), %	38	37	24
UP (CYTO specific), %	83	81	69
DOWN (CYTO specific), %	62	63	76

Fig. 3 | Impaired ribosome biogenesis leads to increased translation in HSPC. **a** Polysome profiles from ckit$^+$ and Ter119$^+$ cell populations in E15.5 control, *Rps19*$^{lox/+}$ or *Rpl5*$^{lox/+}$ embryos. **b** Quantification of the 40S and 60S ribosomal subunits, monosomes (80S) and polysomes expressed as ratio from ckit$^+$ and Ter119$^+$ cell populations in E15.5 control, *Rps19*$^{lox/+}$ or *Rpl5*$^{lox/+}$ embryos. Statistical analysis was performed using two-tailed paired t-test. **c** Quantification of global translation of LSK and Ter119$^+$ populations as measured by OPP in E13.5 control, *Rps19*$^{lox/+}$ or *Rpl5*$^{lox/+}$ embryos. Statistical analysis was performed using two-tailed unpaired t-test. **d** Differential Expression (DE) analyses on the whole cytoplasmic (CYTO) lysate (transcription) and polysomal (POLY) fractions (translation) from Ter119$^+$ cells in E15.5 control, *Rps19*$^{lox/+}$ or *Rpl5*$^{lox/+}$ embryos. **e** Differential Expression (DE) analyses on the whole cytoplasmic (CYTO) lysate (transcription) and polysomal (POLY) fractions (translation) from cKit$^+$ HSPCs in E15.5 control, *Rps19*$^{lox/+}$ embryos. **f** Quantification of genes up or down regulated at the transcriptional and/or translational level in cKit$^+$ and Ter119$^+$ populations at E15.5. % of total is shown. The number of biological replicates (*n*) is indicated in italics under each histogram. All data are presented as mean ± standard deviation. Source data are presented in Source Data file.

analyses of several key factors involved in translation (Supplementary Fig. 3b) at E15.5 and E17.5. The expression of initiation factors involved in CAP-dependent translation[25] were increased (eIF4H) or unaffected (eIF4E, eIF4G) in the *Rps19*$^{lox/+}$ c-kit$^+$ population at E15.5 and E17.5 (Supplementary Fig. 3c–f) while they were significantly decreased in *Rpl5*$^{lox/+}$ c-kit$^+$ HSPC (Supplementary Fig. 3c–f). Interestingly, a transient increase was observed at E15.5 in the ratio p-eIF2α /eIF2α in the *Rpl5*$^{lox/+}$ model compared to their littermate controls, suggesting activation of the integrated stress response[26] (Supplementary Fig. 3c–f).

Recently, eIF5a and its post-translational hypusination, emerged as a regulator of human erythropoiesis[27]. Hypusinated-eIF5a (eIF5a^H) is involved in ribosome functions, preventing ribosome stalling in translation initiation, elongation and termination[28–30]. We previously showed that defects in ribosome biogenesis led to ineffective erythropoiesis in cellular models of ribosomopathies[27,31]. Therefore, we measured the expression levels of eIF5a and eIF5a^H in our models. The ratio of eIF5a^H/eIF5a was specifically elevated in c-kit+ HSPC from *Rps19*$^{lox/+}$ mice but not in c-kit+ HSPC from *Rpl5*$^{lox/+}$ mice compared to littermate controls at E15.5. In addition, the eIF5a^H/eIF5a ratio was subsequently reduced at E.17.5 in the *Rpl5*$^{lox/+}$ mice supporting a specific role for eIF5a^H depending on the RP mutated (Supplementary Fig. 3c–f). Together, these data suggest that HSPCs attempt to compensate for the ribosomal defects by enhancing translation. However, this compensation may be maladaptive and drive HSPC depletion.

Transcriptome and translatome differ in *Rps19*$^{+/-}$ and *Rpl5*$^{+/-}$ models

These data led us to hypothesize that the translational activity would be differentially affected depending on which RP subunit was deleted. To address this, we performed polysome sequencing, which provides insights into translation efficiency by analyzing the distribution of mRNAs across actively translating ribosomal fractions (polysomes)[32], on c-kit$^+$ and Ter119$^+$ populations from RPS19 and RPL5 haploinsufficient embryos at E15.5. Differential expression (DE) analyses of whole cytoplasmic lysates (transcription) and polysomal fractions (translation) revealed that RPL5 and RPS19 haploinsufficiency in the Ter119$^+$ population primarily caused transcriptional changes (Fig. 3d). Specifically, most mRNAs in Ter119$^+$ cells exhibited concordant changes in both transcription and translation (Both up/down category) or the transcriptional changes in these mRNAs did not affect translation (Cyto up/down category): 83% and 85% of the up-translated mRNAs displayed a corresponding increase in transcription in RPL5 and RPS19 haploinsufficient Ter119$^+$ cells, respectively (Fig. 3f). Furthermore, the majority of the transcriptional changes did not appear to impact translation in these cells as 81% and 83% of the up-transcribed mRNAs showed no corresponding changes in translation. In striking contrast, in c-kit$^+$ HSPC, there was a higher proportion of mRNAs where translational changes occurred independently of transcriptional changes (Poly up/down category) (Fig. 3e, f). Indeed, 50% of the up-translated mRNAs did not display a similar variation in transcript levels. This strongly suggests that translation efficiency is more severely affected in c-kit$^+$ HSPC than in more mature Ter119$^+$ erythroid cells. We confirmed these observations by determining the Log2 of the ratio between Δ(translational changes) and Δ(transcriptional changes) (Log2 Δ(translation)/Δ(transcription)). The Log2 Δ(translation)/Δ(transcription) is increased in *Rps19*$^{lox/+}$ c-kit$^+$ compared to *Rps19*$^{lox/+}$ and *Rpl5*$^{lox/+}$ Ter119$^+$ (Supplementary Fig. 4), confirming a higher variation of translation changes in c-kit$^+$ compared to Ter119$^+$ cells. Unfortunately, we were unable to isolate enough RNA in the polysome fractions from c-kit$^+$ cells from RPL5 mutants in order to determine the effect of the haploinsufficiency on translation in these cells. Altogether, these results suggest that RPS19 haploinsufficiency preferentially causes translational alterations in HSPCs while alterations in Ter119$^+$ are primarily a consequence of transcriptional changes.

Transcription is preferentially disrupted in *Rps19*$^{+/-}$ HSPCs

To further explore how the transcriptional landscape is affected during fetal hematopoiesis in *Rps19* and *Rpl5* mutant mice, we performed single-cell RNA-sequencing (scRNAseq) on unfractionated fetal liver cells isolated at E13.5 from two WT and two mutant embryos for each deletion (Fig. 4a). The results were analyzed using an unsupervised clustering approach previously described[33,34]. Cluster identities were assigned based on the expression of the most highly expressed and cluster-specific marker genes, enabling us to distinguish 18 different populations in agreement with published literature[35,36] (Fig. 4b, and Supplementary Fig. 5a). Comparison of the clusters between *Rps19*$^{lox/+}$ and control littermates based on their gene expression profiles revealed that most alterations were observed in the HSPC, megakaryocyte-erythroid progenitor (MEP), megakaryocyte (Mk) and erythroid progenitor (EP) and proerythroblast (ProE) frequencies (Supplementary Figs. 5b, d). However, the cluster distribution in *Rpl5*$^{lox/+}$ was more similar to that of their littermate controls compared to *Rps19*$^{lox/+}$. This suggests that the different populations were less affected at the transcriptional level by the loss of one *Rpl5* allele (Supplementary Figs. 5c, d). These differences were confirmed using scCODA[37] (Supplementary Table 1). Because *Rps19*$^{lox/+}$ and *Rpl5*$^{lox/+}$ mice present with distinct defects in HSPCs and erythropoiesis, we performed a comparative analysis of differentially regulated pathways between the two genotypes in HSPCs, EP and ProE populations. Based on a false discovery rate (FDR) < 0.05, we observed that only one pathway was statistically different at the HSPC stage, being upregulated in RPL5 and downregulated in RPS19. There were no statistically different changes at the EP stage; and most of the changes were observed in the ProE population (Fig. 4c, d). At the individual gene level, *Cdkn1a*, encoding p21, was highly upregulated in HSPCs from *Rps19*$^{lox/+}$, along with other genes involved in apoptosis such as *Bax*; in contrast, *Rpl5*$^{lox/+}$ exhibited increased expression in the genes encoding the α- and β-globin chains (Fig. 4e). This is consistent with the observation that *Rps19*$^{lox/+}$ HSPCs experience deleterious stress and *Rpl5*$^{lox/+}$ HSPCs exhibit a greater compensatory response to erythropoietic defects.

Taken together, these data suggest that in addition to defects in translation, RP haploinsufficiency perturbs the transcriptional landscape during fetal hematopoiesis; however, its impact on transcription is specific and depends on the RP subunit affected, being more global in *Rps19*$^{lox/+}$ mice than in *Rpl5*$^{lox/+}$ mice.

p53-induced cell death diverges in *Rps19*$^{+/-}$ and *Rpl5*$^{+/-}$ fetal HSPCs

Having established translational and transcriptional alterations in the RPS19 and RPL5 haploinsufficient mice, we sought to understand the molecular mechanisms leading to the HSPC defects in these models. The loss of HSPCs in RPS19 but not in RPL5 haploinsufficient mice led us to hypothesize that their cell cycle dynamics might be different. To test this, we analyzed the cell cycle characteristics of HSPCs isolated from E13.5 fetal liver cells using EdU and DAPI (Fig. 5a). All *Rps19*$^{lox/+}$ progenitors—including Lin$^-$ and LSK cells—exhibited G1 accumulation. However, consistent with the accumulation of progenitors in RPL5-haploinsufficient mice, cell cycle entry in *Rpl5*$^{lox/+}$ LSK progenitors was maintained. Indeed, in *Rpl5*$^{lox/+}$ fetal liver cells, defective cell cycle entry was only detected in the Ter119$^+$ compartment (Fig. 5b, and Supplementary Fig. 6a). Furthermore, the rate of EdU incorporation during S phase, indicative of S phase speed, was augmented in all *Rps19*$^{lox/+}$ progenitors but significantly attenuated in *Rpl5*$^{lox/+}$ progenitors (Fig. 5c, and Supplementary Fig. 6b). These data reveal marked differences in the cell cycle dynamics of RPS19- and RPL5-haploinsufficient fetal progenitors, with the former cycling more rapidly and the latter more slowly.

Current understanding of a principal mechanism by which ribosomopathies disrupt the normal behavior of cells is that activation of

https://doi.org/10.1038/s41467-026-71727-y

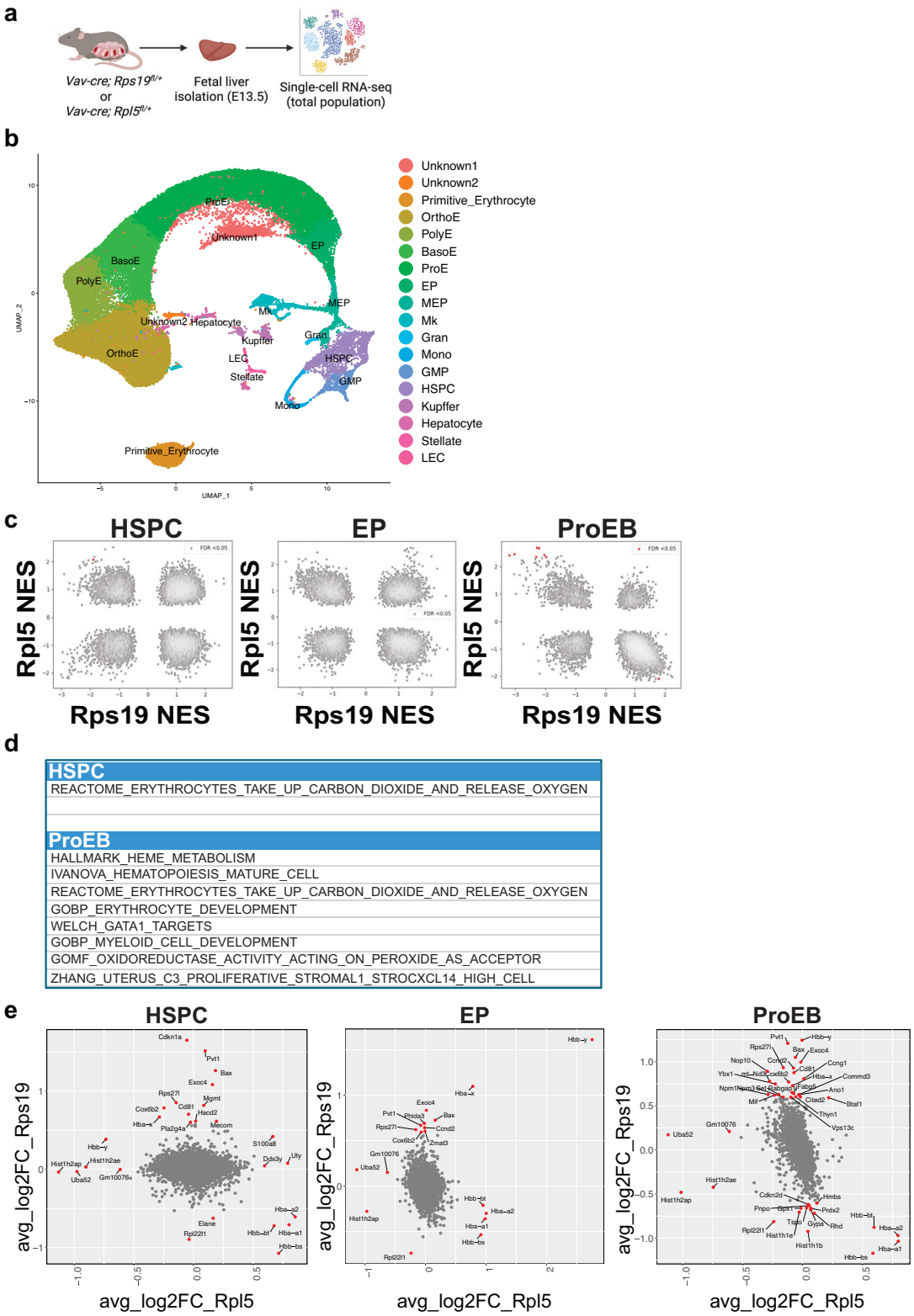

Fig. 4 | scRNAseq analyses unravel global transcriptional defects in *Rps19*$^{lox/+}$ mice. a Experimental design for the scRNAseq (10x Genomics) that was performed on total fetal liver cells from E13.5 embryos. Created in BioRender. Blanc, L. (https://BioRender.com/9sp08pe). **b** scRNA-seq UMAP of integrated FL from control and *Rps19*$^{lox/+}$ and *Rpl5*$^{lox/+}$ cells with clusters identified by marker genes. **c** Concordance analysis of GSEA pathways between *Rps19*$^{lox/+}$ and *Rpl5*$^{lox/+}$ models in HSPC, EP and ProE. **d** List of overlapped significantly enriched pathways (FDR < 0.05) highlighted in red in plot in (**c**). **e** Scatterplots depicting differential expression patterns of the most significantly altered genes between the *Rps19*$^{lox/+}$ and *Rpl5*$^{lox/+}$ mouse models in HSPC, EP and ProE. Source data are presented in Source Data file.

https://doi.org/10.1038/s41467-026-71727-y

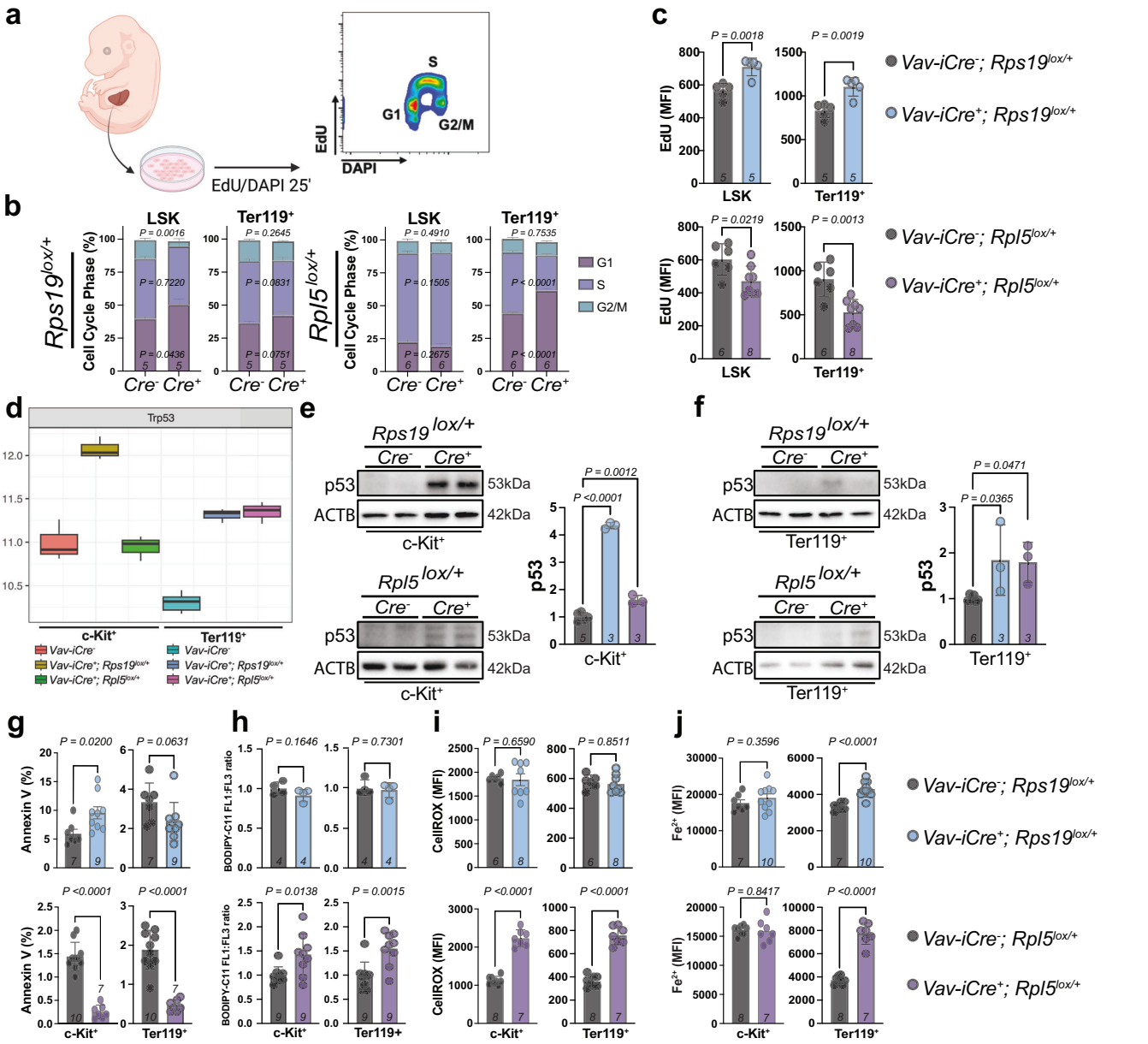

Fig. 5 | G1 accumulation and p53 activation lead to distinct mechanisms of hematopoietic cell death in *Rps19* and *Rpl5* haploinsufficiency. a Experimental design of EdU incorporation in FL cells and cell cycle analysis. Created in BioRender. Blanc, L. (https://BioRender.com/dcasbh7). **b** G1, S and G2/M phase distribution in LSK and Ter119$^+$ populations in E13.5 control, mutant *Rps19*$^{lox/+}$ or mutant *Rpl5*$^{lox/+}$ embryos. Statistical analysis was performed using welch t-test with Holm-Šídák correction. **c** Quantification of the cell cycle speed by measuring the S phase (EdU$^+$) MFI among the LSK and Ter119$^+$ populations in E13.5 control, *Rps19*$^{lox/+}$ or *Rpl5*$^{lox/+}$ embryos. Statistical analysis was performed using two-tailed unpaired t-test. **d** Expression levels of *Trp53* in cKit$^+$ and Ter119$^+$ populations in E15.5 control, *Rps19*$^{lox/+}$ or *Rpl5*$^{lox/+}$ embryos. Data are presented as median (center line), interquartile range (25th–75th percentiles), and whiskers extending to 1.5× the interquartile range. $n = 3$ (**e**) Western blot analysis of p53 and β-actin and quantification of p53 normalized to β-actin in FL- derived ckit$^+$ cells from E15.5 control versus *Rps19*$^{lox/+}$ embryos. Statistical analysis was performed using two-tailed unpaired t-test. **f** Western blot analysis of p53 and β-actin and quantification of p53 normalized to β-actin in FL- derived ckit$^+$ cells from E15.5 control versus *Rpl5*$^{lox/+}$ embryos. Statistical analysis was performed using two-tailed unpaired t-test. **g** Percentage of Annexin V$^+$ cells as marker of apoptosis in E15.5 control, *Rps19*$^{lox/+}$ or *Rpl5*$^{lox/+}$ embryos. Statistical analysis was performed using two-tailed paired t-test. **h** Quantification of cellular lipid peroxidation level of cKit$^+$ and Ter119$^+$ populations measured by the ratio of oxidized and non-oxidized BODIPY dye in E15.5 control, *Rps19*$^{lox/+}$ or *Rpl5*$^{lox/+}$ embryos. Statistical analysis was performed using two-tailed unpaired t-test. **i** Quantification of cellular ROS levels of cKit$^+$ and Ter119$^+$ populations as measured by CellROX dye in E15.5 control, *Rps19*$^{lox/+}$ or *Rpl5*$^{lox/+}$ embryos. Statistical analysis was performed using two-tailed unpaired t-test. **j** Quantification of ferrous iron levels of cKit$^+$ and Ter119$^+$ populations measured as by Fe^{2+} biotracker dye in E15.5 control, *Rps19*$^{lox/+}$ or *Rpl5*$^{lox/+}$ embryos. Statistical analysis was performed using two-tailed unpaired t-test. The number of biological replicates (*n*) is indicated in italics under each histogram. All data are presented as mean ± standard deviation. Source data are presented in Source Data file.

nucleolar stress—mediated by accumulation of 5S-RPL11- RPL5 particles—leads to cell cycle block in G1 due to p53 activation, and apoptotic cell death[38]. The differences observed in G1 accumulation at different stages between the two models led us to interrogate the levels of p53 in the HSPC and Ter119$^+$ populations. There was a 4-fold increase in the levels of p53 in cKit$^+$ HSPC in RPS19 haploinsufficient cells, while p53 in *Rpl5*$^{lox/+}$ mice was only slightly increased compared to littermate controls (Fig. 5d, e). In contrast, in both RPS19 and RPL5 haploinsufficient Ter119$^+$ populations exhibited a comparable and significant increase in p53 expression (Fig. 5d, f).

Having demonstrated a block in G1 and increased p53 expression in both models, albeit at different stages of differentiation, we assessed the level of apoptosis in the different HSPC populations. *Rps19*$^{lox/+}$ mice presented with significant increases in apoptosis at E15.5—measured as a function of Annexin V staining—in HSPC subsets but not in Ter119^{+} cells (Fig. 5g, and Supplementary Fig. 6c) and validating our scRNAseq data, that demonstrated increased expression in genes related to apoptosis (Fig. 4e). Surprisingly, and contrary to previously published studies, all populations of *Rpl5*$^{lox/+}$ cells, including Ter119+ erythroblasts, exhibited significantly lower levels of apoptosis (Fig. 5g, and Supplementary Fig. 6c). Collectively, these results strongly suggest that the depletion of HSPCs in *Rps19*$^{lox/+}$ mice is primarily due to a p53-induced cell cycle arrest and cell death. In contrast, RPL5 haploinsufficiency does not alter cell cycle dynamics in HSPCs. Indeed, these cells exhibit decreased apoptosis relative to their WT counterparts.

As increased p53 expression has been linked to ferroptosis which recently emerged as an alternative mechanism of cell death following ribosomal and oxidative stress[39,40], we hypothesized that ferroptosis was involved in the loss of Rpl5lox/+ Ter119+ cells. Consistent with this, scRNAseq analyses demonstrated an upregulation of pro-ferroptosis genes and downregulation of anti- ferroptosis genes as cells progressed towards erythroid differentiation in RPL5, but not in RPS19 haploinsufficient mice (Supplementary Fig. 7a). Western blots were performed on cKit+ and Ter119+ cells from both models, confirming the scRNAseq data (Supplementary Figs. 7b, c). To further assess how these changes in gene expression affected the cells, we assessed oxidative stress, Fe2+ accumulation and lipid peroxidation (as measured by the ratio BODIPY C:11/C:1340) in RPS19 and RPL5 haploinsufficient mice. While neither oxidative stress nor Fe2+ accumulation or lipid peroxidation was augmented in Rps19lox/+ progenitors, they were significantly augmented in Ter119+ erythroblasts from Rpl5lox/+ animals (Fig. 5h-j, Supplementary Fig. 6d, e).

Thus, the RPS19 and RPL5 haploinsufficient models exhibit divergent and differentiation stage- specific responses downstream of p53 activation: RPS19-haploinsufficient HSPC undergo apoptosis, whereas RPL5-haploinsufficient EPs undergo ferroptosis resulting from oxidative stress.

p53 KO rescues hematopoiesis in both models by distinct mechanisms

To directly assess the contribution of *Trp53* to the hematopoietic failure observed in RPS19 and RPL5 haploinsufficient models, we bred *Vav-Cre; Rps19*$^{lox/+}$ and *Vav-Cre; Rpl5*$^{lox/+}$ mice to *Trp53*$^{fl/fl}$ mice. In the context of RPS19 haploinsufficiency, survival was improved in a dose-dependence manner (Fig. 6a), with the loss of one allele of *Trp53* increasing survival from 10 to 28 days and the loss of both alleles fully rescuing survival. Surprisingly, histological analyses showed that the bone marrow remained hypocellular in the double heterozygous mice, and that the partial rescue could be attributed to splenic stress erythropoiesis (Fig. 6b, c). Indeed, terminal erythroid differentiation in the bone marrow remained significantly impaired (Fig. 6d). In accord with these data, red cell counts were reduced and both the MCV and reticulocyte counts were increased (Fig. 6e). While the recovery was not sustained—mice still died by 4 weeks of age (Fig. 6a), these data highlight a potential role for p53 in stress erythropoiesis. Remarkably, the complete loss of *Trp53* in the *Rps19*$^{lox/+}$ mice led to the complete normalization of the numbers of HSPCs (Fig. 6f), and terminal differentiation was improved, ultimately rescuing survival (Fig. 6a, g).

In the context of RPL5 haploinsufficiency, in marked contrast to the *Rps19* haploinsufficient model, deletion of one allele of *Trp53* in the *Rpl5*$^{lox/+}$ mice did not improve their survival (Fig. 6h), suggesting that, in double heterozygous mice, stress erythropoiesis is not activated or cannot sufficiently compensate for the anemia observed *in utero*. However, deletion of both alleles of *Trp53* rescued their survival (Fig. 6h). Unlike *Rps19* haploinsufficient mice, HSPC numbers remained unaffected by the deletion of *Trp53*, except for the LT-HSC, which were reduced to levels comparable to littermate controls (Fig. 6i). Nevertheless, the complete deletion of *Trp53* in the *Rpl5*$^{lox/+}$ model was associated with a complete recovery of the number of Ter119^{+} cells, and improvement of terminal erythroid differentiation, suggesting that loss of *Trp53* led to the rescue of erythropoiesis (Fig. 6j). In aggregate, these data demonstrate that *Trp53* rescues survival through distinct mechanisms in RPS19 and RPL5 haploinsufficient mice.

RUNX1 is involved in HSPC depletion in RPS19 haploinsufficiency

Since RPS19 and RPL5 haploinsufficiencies appear to disrupt different signaling pathways downstream of *Trp53* and that its deletion rescues hematopoiesis through different mechanisms, we next sought factors that might explain the divergent phenotypes RPS19 and RPL5 haploinsufficient models. Previous studies have suggested a role for the transcription factor RUNX1 in ribosome biogenesis and translation and have demonstrated reduced p53 activation and apoptosis in *Runx1* knockout HSPCs[41,42]. Further, single-sample GSEA (ssGSEA) from our polysome sequencing experiments showed increased activity in RUNX1 targets involved in HSC differentiation (Supplementary Fig. 8a). Interestingly, we observed increased expression of *Runx1* in *Rps19*$^{lox/+}$ in HSPC and downstream erythroblast populations while it was decreased in *Rpl5*$^{lox/+}$ compared to littermate controls (Supplementary Fig. 8b). Furthermore, western blot analysis of c-kit^{+} cells at E15.5 confirmed a striking increase in expression of RUNX1 in *Rps19*$^{lox/+}$ compared to littermate controls but not in *Rpl5*$^{lox/+}$ embryos, suggesting that *Runx1* does not play a significant role in RPL5 haploinsufficiency (Fig. 7a). Based on these data, we investigated whether knocking out *Runx1* in HSCs would rescue the hematopoietic defects in *Rps19*$^{lox/+}$ mice. To this end, we bred *Runx1*$^{fl/fl}$ mice to the *Vav-Cre; Rps19*$^{lox/+}$ and monitored survival. While double heterozygous mice were born, they did not reach weaning age, and none of the mice in which two copies of *Runx1* had been conditionally deleted in the *Rps19*$^{lox/+}$ background were born (Supplementary Fig. 8c). We then assayed erythropoiesis, and in the E15.5 embryos we observed that the fetal liver cellularity was unchanged compared to the *Rps19*$^{lox/+}$. Similarly, Lin^{-} cells were unaffected by the removal of one or two copies of *Runx1*. Strikingly however, there was a partial rescue of the HSPC compartment, with significant increased numbers of LT-HSC and MPPs (Fig. 7b). Of note, terminal erythropoiesis was significantly worsened in the absence of *Runx1* (Supplementary Fig. 8d), suggesting that these mice died of erythropoietic failure.

To understand the relationship between *Trp53* and *Runx1* in the molecular mechanism leading to hematopoietic failure in the *Rps19*$^{lox/+}$ animals, we performed combined scRNAseq and scATACseq analyses using the *Vav-Cre*$^{+}$*; Rps19*$^{lox/+}$*, p53*$^{lox/+}$ mice versus controls. We reasoned that since deletion of one allele of *Trp53* did not correct the HSPC defects (Fig. 6), using these animals would limit confounders in a potential role for *Runx1*. UMAP representation of the scRNAseq integrated results, density projection of each individual dataset and GSEA confirmed alterations in the HSPC subsets in the *Vav-Cre*$^{+}$*; Rps19*$^{lox/+}$ compared to the control littermates (Supplementary Figs. 9a, b). The *Rps19*$^{lox/+}$*, p53*$^{lox/+}$ HSPC presented with significant positive enrichments in GSEA involved in ribosome biogenesis among others (Supplementary Figs. 9c, d).

To identify transcription factors that may have contributed to the rescue of the HSPC phenotype in *Rps19*$^{lox/+}$*, p53*$^{lox/+}$ we characterized regions that underwent chromatin accessibility changes using our scATACseq results from the same three conditions (Fig. 7c, d) using the Cistrome Gene Analysis Toolkit (http://dbtoolkit.cistrome.org/)[43]. We first identified differential open chromatin region (OCR) modules (more accessible or less accessible) in each condition. We then

https://doi.org/10.1038/s41467-026-71727-y

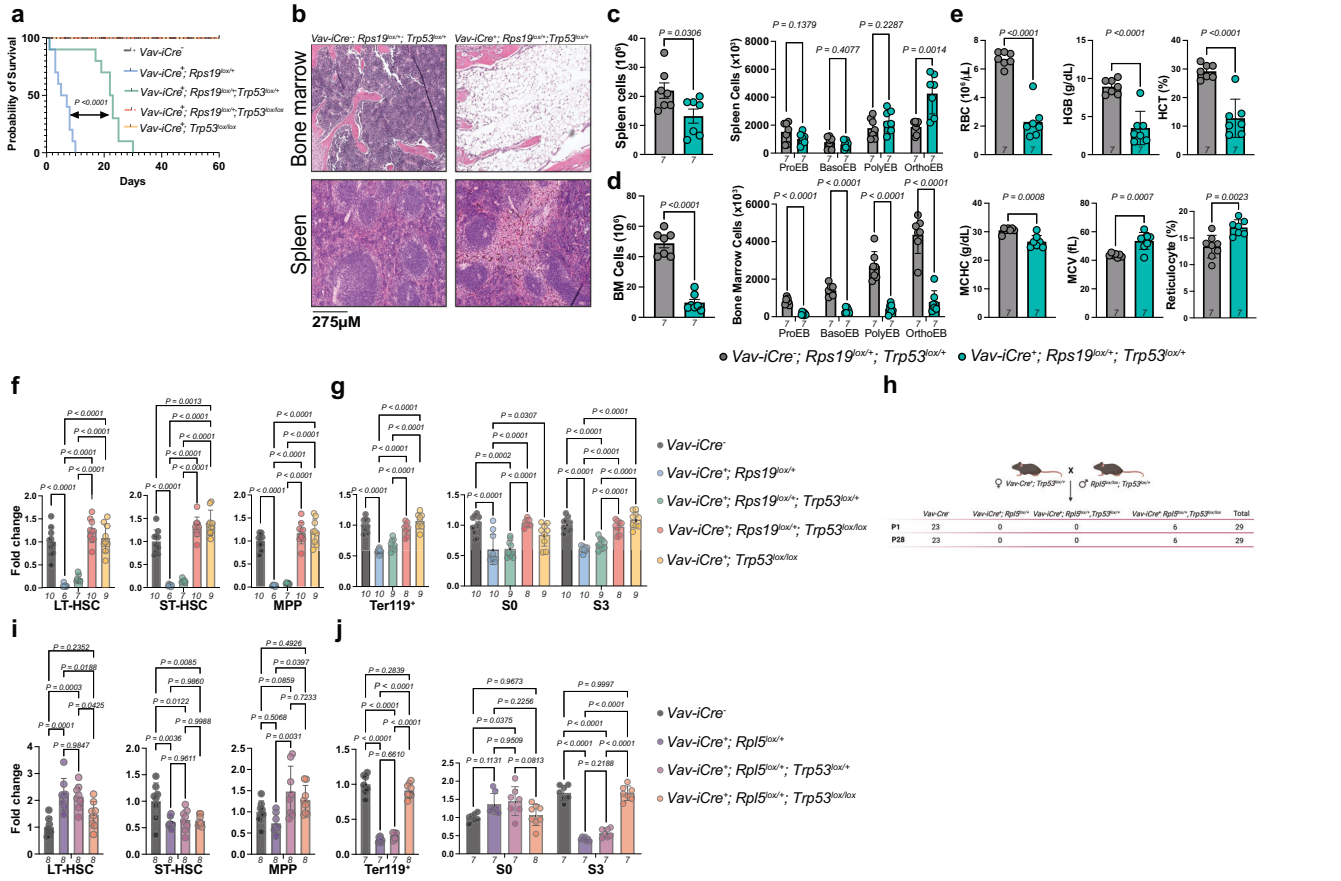

Fig. 6 | Rescue of the hematopoietic defects in both RP insufficient models require the complete ablation of p53. a Survival curves from control, *Rps19*$^{lox/+}$, *Rps19*$^{lox/+}$*; p53*$^{lox/+}$, *Rps19*$^{lox/+}$*; p53*$^{lox/lox}$ and *p53*$^{lox/lox}$ mice. Statistical analysis was performed using Mantel-Cox log rank test. **b** Light microscopy images highlighting the architecture and cellular composition of the bone marrow (BM) and spleen in control and *Rps19*$^{lox/+}$*; p53*$^{lox/+}$mice at P21. Images are representative of 3 independent experiments. **c** Spleen cellularity and quantification of terminal erythropoiesis by flow cytometry based on CD44/Ter119/FSC as markers of differentiation in control and *Rps19*$^{lox/+}$*; p53*$^{lox/+}$mice at P21. Statistical analysis was performed using two-tailed unpaired t-test. **d** BM cellularity and quantification of terminal erythropoiesis by flow cytometry based on CD44/Ter119/FSC as markers of differentiation in control and *Rps19*$^{lox/+}$*; p53*$^{lox/+}$mice at P21. Statistical analysis was performed using multiple two-tailed unpaired t-test. **e** Red cell parameters at P21. Upper panel: red blood cells (RBC), hemoglobin (HGB), hematocrit (HCT). Lower panel: mean corpuscular hemoglobin concentration (MCHC), mean corpuscular volume (MCV), reticulocytes. Statistical analysis was performed using two-tailed unpaired t-test. **f** Quantification of the different HSPC populations in E17.5 control, *Rps19*$^{lox/+}$, *Rps19*$^{lox/+}$; *Rps19*$^{lox/+}$, *Rps19*$^{lox/+}$*; p53*$^{lox/+}$, *Rps19*$^{lox/+}$*; p53*$^{lox/lox}$ and *p53*$^{lox/lox}$ embryos expressed as a fold change relative to control. Statistical analysis was performed using ordinary one-way ANOVA with Tukey correction. **g** Ter119+ cell counts and quantification of cells in S0 and S3 in E17.5 control, *Rps19*$^{lox/+}$, *Rps19*$^{lox/+}$*; p53*$^{lox/+}$, *Rps19*$^{lox/+}$*; p53*$^{lox/lox}$ and *p53*$^{lox/lox}$ embryos expressed as a fold change relative to control. Statistical analysis was performed using ordinary one-way ANOVA with Tukey correction. **h** Genotype counts from *Rpl5*$^{lox/+}$*; p53*$^{lox/lox}$ intercrossing. Created in BioRender. Blanc, L. (https://BioRender.com/ql4svuv). **i** Quantification of the different HSPC populations in E17.5 control, *Rpl5*$^{lox/+}$, *Rpl5*$^{lox/+}$*; p53*$^{lox/+}$ and *Rpl5*$^{lox/+}$*; p53*$^{lox/lox}$ embryos expressed as a fold change relative to control. Statistical analysis was performed using ordinary one-way ANOVA with Tukey correction. **j** Ter119+ counts and quantification of cells in S0 and S3 in E17.5 control, *Rpl5*$^{lox/+}$, *Rpl5*$^{lox/+}$*; p53*$^{lox/+}$ and *Rpl5*$^{lox/+}$*; p53*$^{lox/lox}$ embryos expressed as a fold change relative to control. Statistical analysis was performed using ordinary one-way ANOVA with Tukey correction. The number of biological replicates (*n*) is indicated in italics under each histogram. All data are presented as mean ± standard deviation. Source data are presented in Source Data file.

assessed the TF and chromatin regulator enrichment score (Giggle score) in the OCRs, which identifies enriched motifs for known transcriptional regulators by comparing the input file to thousands of reference files from databases such as ENCODE[44]. The Cistrome analysis (Fig. 7e) suggests that regions of GATA1/LDB1/LMO2/TAL1/P300 complex occupancy lose accessibility in *Vav-Cre*$^{+}$*; Rps19*$^{lox/+}$ HSPCs, which is consistent with the subsequent effect on erythropoiesis. Notably, *Trp53* is the most enriched factor in the more accessible regions as expected. Interestingly, RUNX1 is enriched in the differential OCRs, highlighting the dysregulation of RUNX1 regulatory network in the context of RPS19 haploinsufficiency. Published ChIP-seq data from mouse bone marrow and HSPCs[45,46] confirmed the binding of RUNX1 on the *Cdkn1a* gene (Supplementary Fig. 9e). Further analyses of the scATACseq results showed that the RUNX1 (MA0002.3) motif exhibits a slight skewing towards negative in both *Rps19*$^{lox/+}$ HSPCs and *Rps19*$^{lox/+}$*; tp53*$^{lox/+}$ HSPCs. However, the presence of longer tails suggests an increase in variability; a small subset showing enhanced accessibility (Fig. 7f, and Supplementary Fig.9f, g). Taken together, these results demonstrate that RUNX1 could play a role in the mechanism of HSPC failure in RPS19 haploinsufficiency through direct binding to the *Cdkn1a* promoter. Since we could not perform ChIP-seq analyses due to the low number of cells in the haploinsufficient conditions, we also carried out western blot assays on the c-Kit^{+} fraction at E15.5. We observed that while the p21 expression levels were dramatically reduced in the absence of *Runx1*, the levels of p53 remained unchanged (Fig. 7g, h). Conversely, in the *Rps19*$^{lox/+}$*; Trp53*$^{lox/lox}$ c-Kit+ cells, the levels of RUNX1 were back to baseline levels, suggesting that Trp53 is upstream of Runx1 (Fig. 7i). Together, these results indicate that RUNX1 acts between p53 and p21 in the mechanism leading to hematopoietic failure in *Rps19*$^{lox/+}$.

Finally, as proof of principle about the direct relevance of these findings to human DBAS, we investigated the expression of RUNX1 in

https://doi.org/10.1038/s41467-026-71727-y

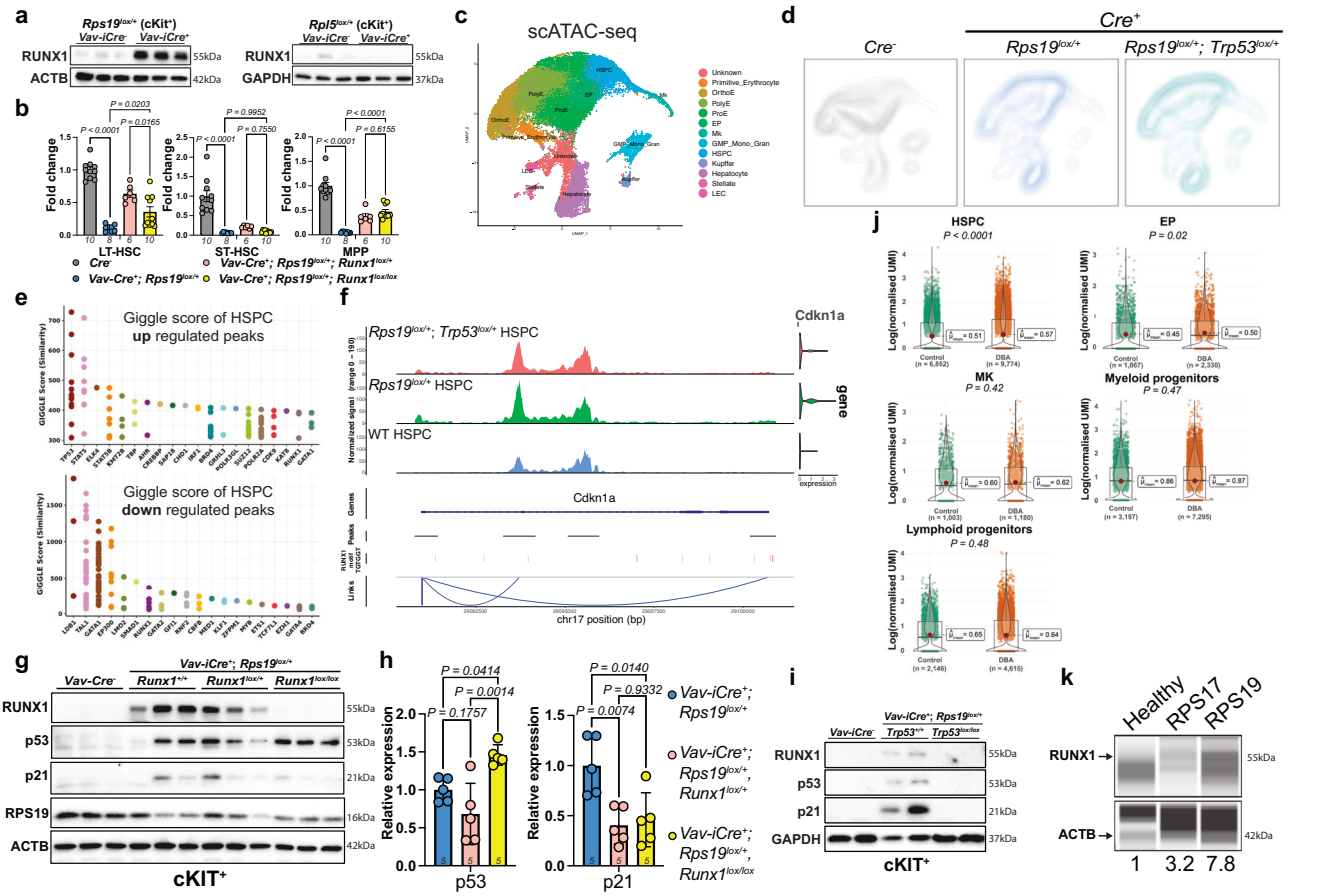

Fig. 7 | Role of RUNX1 in RPS19 haploinsufficiency. a Western blot analyses of RUNX1 expression in ckit$^+$ cells from E17.5 control and *Rps19*$^{lox/+}$ and *Rpl5*$^{lox/+}$ embryos. $n = 3$ mice per group. **b** FL cellularity and quantification of the different HSPC populations in E17.5 control, *Rps19*$^{lox/+}$, *Rps19*$^{lox/+}$*; Runx1*$^{lox/+}$ and *Rps19*$^{lox/+}$*; Runx1*$^{lox/lox}$ embryos expressed as a fold change relative to control. Statistical analysis was performed using ordinary one-way ANOVA with Tukey correction. **c** scATAC-seq UMAP of integrated E13.5 FL from control, *Rps19*$^{lox/+}$ and *Rps19*$^{lox/+}$*; p53*$^{lox/+}$ cells with clusters identified by marker genes. **d** Density projection of cells on scATAC-seq UMAP from control, *Rps19*$^{lox/+}$ and *Rps19*$^{lox/+}$*; p53*$^{lox/+}$ FL cells at E13.5. **e** Differential open chromatin regions are separated into more accessible group (upregulated) and less accessible group (downregulated). The GIGGLE score of 20 predicted transcription factors is displayed in each group. **f** Genome Browser snapshot of the ATAC-seq signal at the *Cdkn1a* gene locus in HSPCs. *Runx1* binding motif (TGTGGT) is highlighted and bottom tracks are analyzed using Signac. **g** Western blot analysis of RUNX1, p53, p21 and RPS19 in FL-derived ckit$^+$ cells from E17.5 control, *Rps19*$^{lox/+}$, *Rps19*$^{lox/+}$*; Runx1*$^{lox/+}$ and *Rps19* $^{lox/+}$*; Runx1*$^{lox/lox}$ embryos. **h** Quantification of the western blots for p53 and p21 in *Rps19*$^{lox/+}$, *Rps19*$^{lox/+}$*; Runx1*$^{lox/+}$ and *Rps19*$^{lox/+}$*; Runx1*$^{lox/lox}$ ckit$^+$ cells, normalized to control. Statistical analysis was performed using ordinary one-way ANOVA with Tukey correction. **i** Western blot analysis of RUNX1, p53, p21 and RPS19 in FL-derived ckit$^+$ cells from E17.5 control, *Rps19*$^{lox/+}$, and *Rps19*$^{lox/+}$*; p53*$^{lox/lox}$ embryos. $n = 2$ mice per group. The number of biological replicates (n) is indicated in italics under each histogram. all data are presented as mean ± standard deviation. **j** Violin plots depicting expression of *RUNX1* within stem and progenitor cells from control ($n = 3$) and DBAS ($n = 6$) patients BM, analyzed ex vivo. n refers to total number of cells and data are presented as mean (red dots) ± standard error of the mean with individual data points overlaid. Box plots indicate median and interquartile range, with whiskers showing the full data range. Statistical analysis was performed using Wilcoxon rank test (non parametric). **k** Capillary western blot analysis of RUNX1 and β-actin in CD34+ cells from healthy donors and DBAS patients with a mutation in *RPS17* or *RPS19*. Values on the X-axis represent the fold change of RUNX1 expression normalized by β-actin level. Each lane represents one patient. Source data are presented in Source Data file.

primary bone marrow HSPCs from patients with DBAS by reanalyzing a recently published dataset[47]. This showed a selective increase in *RUNX1* expression in HSPC and EPs but not myeloid or lymphoid progenitors or megakaryocytes in patients with DBAS compared to age-matched controls (Fig. 7j). We further confirmed elevated expression levels of RUNX1 in undifferentiated CD34$^+$ cells directly isolated from patients compared to CD34$^+$ cells from healthy controls (Fig. 7k). Altogether, these results suggest that RUNX1 plays a role in HSPC depletion in RPS19 haploinsufficiency and that this mechanism may be conserved in patients with DBAS.

Discussion

Here, we provide a comprehensive evaluation of the role of the ribosomal proteins RPS19 and RPL5 during fetal hematopoiesis in mice with a focus on erythropoiesis and offer a mechanistic explanation at the functional and molecular level for the differences observed in patients with RPS and RPL ribosomopathies. Using two clinically relevant models of DBAS, we demonstrate that while they both have a similar anemic phenotype, the severity and mechanisms are different and distinct depending on the RP subunit deleted (Fig. 8). We found that although both RP subunits are critical for fetal hematopoiesis, RPS19 is essential from the HSPC stage while RPL5 appears to be critical after erythroid commitment has occurred. We identified different phenotypes in the HSPC compartments, with progressive depletion in the *Rps19*$^{lox/+}$ and expansion in the *Rpl5*$^{lox/+}$ animals. These results uncover fundamental differences in the activity of RPS19 or RPL5 in HSPC compared to the more committed erythroid progenitors. They further our understanding of the role of p53 and unravel a potential function for RUNX1 in the mechanisms leading to DBAS.

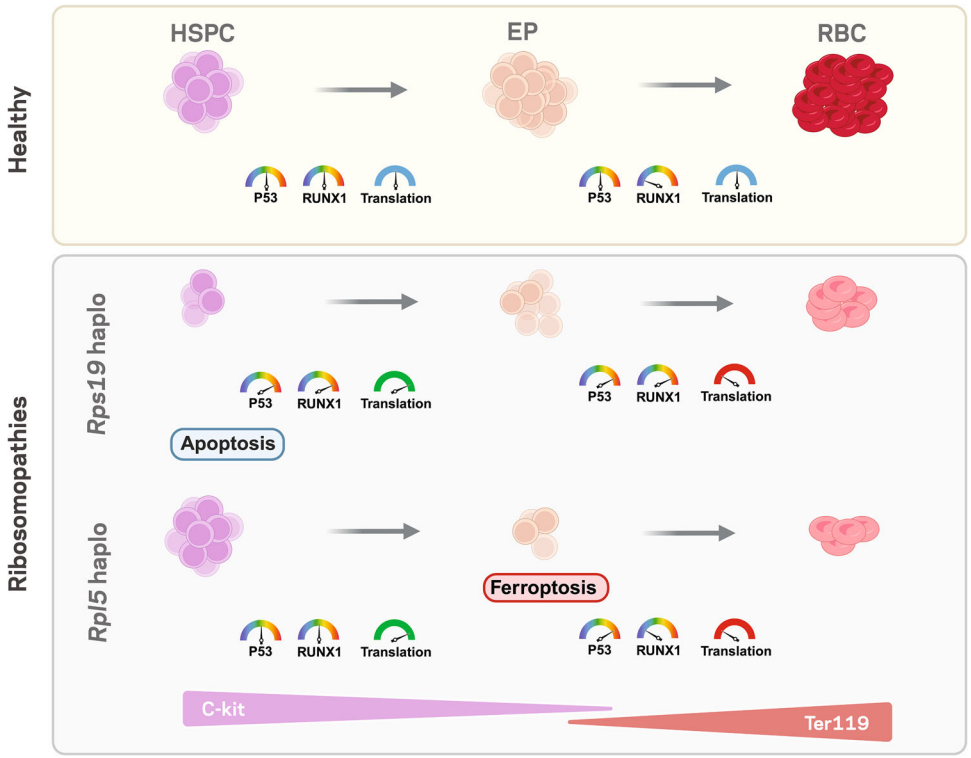

Fig. 8 | Proposed model summarizing the defect in RPS19 and RPL5 haploinsufficiency during fetal hematopoiesis. Created in BioRender. Papoin, J. (https://BioRender.com/6ekncfh).

Focusing on RPS19 and RPL5, as they are the most commonly mutated RPs in ribosomopathies[48], we demonstrated that the removal of one allele during definitive hematopoiesis leads to severe defects with different consequences based on the lineage affected. The pressure was mostly exerted on the erythroid compartment, eventually leading to death due to anemia. Since the liver is the major site of erythropoiesis in fetal life, potential defect in other hematopoietic lineages may be "masked" by the abundance of erythroid cells. However, our scRNAseq studies showed that the fetal myeloid output was not affected in our models, in accordance with recently published studies demonstrating that fetal HSPCs have diminished steady-state myeloid cell production compared with adult HSPCs[49]. Nevertheless, at birth, we noticed pancytopenia in the *Rps19* model, suggesting that RPS19 may play different roles in fetal vs adult HSPCs. Whether the same holds true for *Rpl5* remains unknown, since haploinsufficient RPL5 mice die at birth.

Phenotypically, we observed anemia in both models of haploinsufficiency; however, the mechanisms leading to red cell failure are distinct depending on the RP affected. One possible explanation for the phenotypic differences between RPS19 and RPL5 is the mechanism of cell death. Indeed, *Rps19* haploinsufficient HSPCs had increased apoptosis while in Rpl5 haploinsufficient cells, we observed ferroptosis, which was exacerbated as cells differentiated towards the red cell lineage. This model would be consistent with previous studies demonstrating heme imbalance in patients with DBAS where mutations in genes other than RPS19 were involved[50]. This heme imbalance leads to an excess in free heme, which in turn can activate oxidative stress and ferroptosis[38]. Thus, RPL5 haploinsufficiency could result in accumulation of free heme leading to ferroptosis and progressive cell death, an accumulation of cells in S0 (erythroid progenitors), and a block in terminal erythroid differentiation. In contrast, Rps19 haploinsufficiency causes HSPC death by apoptosis leading to progressive depletion of the HSPC compartment. However, cells that are able to reach the erythroid progenitor stage can differentiate up to the S3 (polychromatophilic) stage where a second defect causes severe erythropoietic failure in both models.

Our findings clarify, and reconcile, the role of different factors previously implicated in DBAS. Indeed, studies have proposed a mechanism converging on the defective translation of GATA1 in the erythroid compartment[51], while others have suggested a role for protein chaperones[50], heme imbalanced production[52], or *trp53*[8] among others. Many of these studies were performed in vitro, using shRNA technologies to knock down RPs or using cells isolated from patients, with the caveat that very few HSPCs could be recovered. Using our in vivo models, we demonstrate that indeed, heme synthesis is more affected in RPL5 than in RPS19 haploinsufficient mice and that GATA1 is essential to the defects observed in the erythropoietic failure, although it is not centralto the disease, since in the RPS19 haploinsufficient model, the defect originates at a stage prior to GATA1 expression. Our findings complement and expand recent ex vivo studies showing two distinct cellular trajectories segregating with the ribosomal subunit mutated[47].

These RPS19 and RPL5 haploinsufficiency models recapitulate more accurately DBAS in the sense that reticulocytosis does not occur, due to the absence of stress erythropoiesis in the spleen. Indeed, in other murine models of bone marrow failure or anemia, extramedullary erythropoiesis occurs in the spleen, compensating for the failure in red cell production in the marrow, and confounding some of the findings[53–55]. To our knowledge, the ISAM mouse, a model of EPO deficiency, is the only model of impaired erythropoiesis without splenomegaly[56]. The absence of stress erythropoiesis enabled us to unravel a role for p53 in this process with a specificity for the RP deleted. Indeed, the ablation of one allele led to an increase in survival in $Rps19^{lox/+}$ mice, but not in the $Rpl5^{lox/+}$ model. Our data demonstrate a rescue of terminal erythroid differentiation in the spleen of $Rps19^{lox/+}$ pups, partially compensating for the anemia. However, the complete absence of erythropoiesis in the bone marrow points towards different p53-dependent mechanisms in blood cell production depending on

the anatomical site. Further, it suggests that stress erythropoiesis in the spleen originates from a pool of EPs already present, the so-called stress BFU-E[57], unlike the marrow pool, which originates from HSC.

With regards to the role of p53 in ribosomal stress during fetal hematopoiesis, both models demonstrate increased p53 expression and its associated targets; however, our polysome- sequencing data in the RPL5 model do not show an increase in the translation of p53, suggesting that the main mechanism at play may reside in its stabilization. We demonstrated that removal of both copies of *Trp53* is necessary for the rescue of the HSPC compartment in the context of RP haploinsufficiency. This suggests that the ribosomal stress experienced by HSPCs is highly sensitive to p53 stability and that its total removal is necessary to bypass it.

We demonstrate that both RPS19 and RPL5 haploinsufficiency cause a decrease in translation in erythroid committed cells. However, this defect is preceded by an increase in protein translation in HSPCs compared to the control littermates, probably contributing to the exhaustion of the HSPC compartment in Rps19lox/+ mice. Although it may seem counterintuitive in the context of RP haploinsufficiency, our data suggest that HSPCs respond to the loss of mature blood cells by increasing differentiation; as this requires more translation[58], the capacity of the HSPC to maintain protein quality and homeostasis, ultimately leads to HSPC depletion[59]. In contrast, in RPL5 haploinsufficiency, depletion of the HSPC compartment may still occur, but later than in the RPS19 haploinsufficient model. At the molecular level, we identified an increase in mTOR signaling pathway activity, which can compensate for defects in ribosome biogenesis, notably through the phosphorylation of 4E-BP1. Upregulation of 4E-BP1 activity was previously described in the context of Rps6 haploinsufficiency during limb development[60], but not in the context of hematopoiesis. Beyond the mTOR signaling pathway, we demonstrate differential hypusination of eIF5A based on the ribosomal subunit deleted. Along with our previous study highlighting the critical nature of eIF5A-dependent mitochondrial function in regulating the erythroid commitment of HSPCs[27] and other studies reporting its role in preventing ribosome stalling[28], our results suggest specific metabolic regulations depending on the subunit affected and illustrate the need for further mechanistic studies for therapeutic applications.

While it expands on findings from other RP deleted in other tissues or during adult hematopoiesis, it will be essential to examine whether our results can be extrapolated to other RP and if observed defects segregate according to whether RP in the small versus large ribosomal subunits are affected. Finally, we unraveled a role for *Runx1* in the RPS19 haploinsufficient model. RUNX1 is known to be involved in defective ribosome biogenesis, and its loss of function was linked to decreased translation in HSPCs[41]. We demonstrate using both genetic and functional approaches that RUNX1 is indeed playing a key role in the defects we observed during fetal hematopoiesis. While the removal of RUNX1 does not rescue erythropoiesis or survival in the RPS19 haploinsufficient mice, it partially rescues the numbers of HSPCs. Recent reports have demonstrated that patients with a mutation or a deletion in a ribosomal protein have a 4- to 5-fold risk of developing cancer[61]. However, the mechanisms leading from a hypoproliferative to a hyperproliferative condition remain unknown[62]. We suggest that the increased expression of RUNX1 could play a role in the mechanism leading to tumorigenesis; however, additional studies are required to explore its role during human hematopoiesis in the context of ribosomal protein haploinsufficiency. Nevertheless, along with the role of p53 in ribosomopathies, this finding could open a new direction towards our understanding of hematologic malignancies in DBAS.

Methods

Antibodies

The following antibodies were used: CD4-BV605 (Biolegend, #100451, 1:200); CD8a-BV6-5 (Biolegend, #100744, 1:200); Ter119-BV605 (Biolegend, #116239, 1:200); CD45R/B220-BV605 (Biolegend, #103224, 1:200); Ly-6G/Ly-6C-BV605 (Biolegend, # 108440, 1:200); c-Kit-APC-eFluor780 (eBioscience, #47-1171-82, 1:200); Sca-1-BV711 (Thermo Scientific, #11-5981-82, 1:200); CD48-AlexaFluor 700 (Biolegend, #103426, 1:200); CD150-BV785 Biolegend, # 115937, 1:200); CD34-PE (BD Biosciences #551387, 1:50); CD34-FITC (BD Biosciences #553733, 1:50); CD16/32-PerCP-Cy5.5 (Thermo Scientific, #45-0161, 1:100); CD71-PE (eBioscience, #12-0711-83, 1:400); CD44-APC (Biolegend, #100412, 1:200); Ter119-FITC (BD Biosciences, #557915, 1:200); CD45R-APC-Cy7 (BD Biosciences, #552094, 1:200); CD11b-APC-Cy7 (BD Bioscience, #557657, 1:200); Ly6G/Ly6C-APC-Cy7 (BD Biosciences, #557661, 1:200); Annexin V-FITC (Biolegend, #640945, 1:200); GAPDH-HRP (Cell Signaling Technologies, #8884, 1:2000); p53 (Cell Signaling Technologies, #2524, 1:1000); Rps19 (Bethyl Labs, #A304-002A, 1:4000); Rpl5 (Abcam, # ab86863, 1:4000); AML1 (Cell Signaling Technologies, #4334, 1:10); RPS6 (Cell Signaling Technologies, #2217, 1:4,000); p-RPS6 (Cell Signaling Technologies, #4858, 1:2000); 4EBP1 (Cell Signaling Technologies, # 9644, 1:1000); p-4EBP1 (Cell Signaling Technologies, #2855, 1:1000); p21 (BD Biosciences, #556431, 1:1000); eEF2 (Cell Signaling Technologies, #2332, 1:1000); p-eEF2 (Cell Signaling Technologies, #2331, 1:1000); eIF2α (Cell Signaling Technologies, #5324, 1:4000); p-eIF2α (Cell Signaling Technologies, #3398, 1:4000); Actin-β (Cell Signaling Technologies, #4970, 1:4000); eIF5a (BD Biosciences, #611976, 1:4000); Hypusine (Creative Biolab, #PABL-202, 1:4000); PABP1 (Cell Signaling Technologies, #4992, 1:1000); eIF4E (Cell Signaling Technologies, #2067, 1:1000); eIF4G (Cell Signaling Technologies, #2469, 1:1000); eIF4H (Cell Signaling Technologies, # 3469, 1:1000); AML (Cell Signaling Technologies, #8529, 1:1000).

Chemicals, peptides, and recombinant proteins

Fetal bovine serum (Cytiva, #SH30071.03); IMDM (Fisher Scientific, #12-440-079); BSA (Fisher Scientific, #BP9703100); PBS (Cytiva, #SH30256.LS); RIPA buffer (Thermo Fisher Scientific, #89900); Agarose (IBI Scientific, #IB70042); Precision Plus Protein Dual Color Standards (BioRad, #1610374); 100 bp DNA Ladder (NEB, #N3231L); Proteinase K (Lamda Biotech, #DB0451-10); O-Propargyl-Puromycin (MedChem Express, #HY-15680); Sucrose (Sigma-Aldrich, #S9378-1KG); RiboSafe RNase Inhibitor (Bioline, #BIO-65028); Cycloheximide (Sigma-Aldrich, #C1988-1G); Sodium Chloride (Alfa Aesar, #12314-A3); Magnesium Chloride (Sigma-Aldrich, #M1028-100ML); DAPI (Sigma-Aldrich, #D9542-10mg); MethoCult M3334 (Stemcell Tech, #M3334); Methocult SF M3436 (Stemcell Tech, #M3436); MethoCult GF M3434 (Stemcell Tech, #M3434); CD117 Microbeads (Miltenyi Biotec, #130-091-224); Anti-Ter-119 MicroBeads (Miltenyi Biotec, #130-049-901); Phosphatase Inhibitor Cocktail (Bio Basic, #PL017); Protease Inhibitor Cocktail (Bimake, #B14002).

Critical commercial assays

Click-iT Plus EdU Assay Kit (Thermo Scientific, #C10632); Chromium Next GEM Single Cell 3' Kit (10X Genomics, #1000268); Chromium Next GEM Single Cell Multiome ATAC+Gene Expression Reagent Bundle (10X Genomics, #1000283); Chromium Next GEM Chip G Single Cell Kit (10X Genomics, #1000120); Single Index Kit N, Set A (10X Genomics, #1000212); Dual Index Kit TT, Set A (10X Genomics, #1000215).

Deposited data

Mouse single cell RNAseq (This paper); Human single cell RNAseq (Iskander et al.[47]); Mouse single cell ATACseq (This paper); Mouse polysome sequencing (This paper).

CD34 + HSPCs isolation

Human $CD34^+$ HSPCs from normal or DBAS patients were isolated from de-identified peripheral blood in accordance with Institutional Review Board approval (#01.10.088 G, Northwell Health).

Mononuclear cells were separated from blood using Lymphoprep (Stem Cell Technologies) and incubated with anti-CD34 magnetic microbeads (Miltenyi Biotec). $CD34^+$ HSPCs were subsequently column purified with MACS columns as per manufacturer's protocol (Miltenyi Biotec).

Generation of the *Rps19*$^{fl/fl}$ and *Rpl5*$^{fl/fl}$ models

Rps19$^{fl/fl}$ mice were generated at Jackson Laboratory through CRISPR/cas9 endonuclease mediatedgenomeeditingoftheRps19 locususingsgRNAsequences (GGGTGGACTGGCGACGAGCA,GGAC TGGCGACGAGCAGGGT,TCTTTTCTGAATTGGGCC TA, AAAGGAA GCATGGTCACCGT).

Rpl5$^{fl/fl}$ mice were generated at Jackson Laboratory through CRISPR/cas9 endonuclease mediated genome editing of the Rpl5 locus using sgRNA sequences (CATTGAAGACTAATCTGTAT, TCATTGAA-GACTAATCTGTA, CACCCTGAGTTCTCTAGTAC, GAACCTGTACTAGA GAACTC).

All mice were housed under alternate dark/night cycle of 12 h at 20 ± 2 °C and 50 ± 10% humidity.

All mice were backcrossed at least ten times onto a C57BL/6 background.

Vav-iCre$^+$ female mice were used for breeding to avoid leakiness of the Vav promoter. Embryos were analyzed independently of their sex. No difference was noted in male or female embryos. Mouse tails were used genotyping. The following primers were used for genotyping: *Rps19* FORWARD (GAACGTGGGCTTGAGGGAGC); *Rps19* REVERSE (GTTTGGCCAGCTTGACTGTG); Rpl5 WT FORWARD (AACCACCATG-TAGTTGATGCC); *Rpl5* WT REVERSE (GCTGACCGTCAATGCTTTCC); *Rpl5* FLOX FORWARD (CCTAAACCACCATGTAGTTGATGA-TAACTTCGTATAATGTAT); *Rpl5* FLOX REVERSE (CAGTGA-GAAAAGTCAGGTTATTAACTTGTTGCTATCA). DNA extraction and isolation from tissues were performed according to manufacturer's instructions (Invitrogen).

The study was reviewed and approved by the Feinstein Institutes IACUC, protocol #2022-019.

Isolation of fetal liver c-kit$^+$ and Ter119$^+$ cells

Fetal liver-derived cells were incubated anti-c-kit magnetic microbeads (Miltenyi Biotec) or anti- Ter119 magnetic microbeads (Miltenyi Biotec) on ice for 15 min, and then c-kit$^+$ and Ter119$^+$ cells were subsequently column purified with MACS columns as per manufacturer's protocol (Miltenyi Biotec). These isolated cells were quickly frozen and then keep at −80 °C before used for western blot. Freshly isolated fetal liver-derived c-kit$^+$ cells and Ter119$^+$ cells were used in the polysome profiling assays.

Histology

Spleens, livers and hindlimbs were isolated and fixed in 10% (vol/vol) formalin. After fixation, hindlimbs were further decalcified using 0.5 M EDTA pH7.2 for one week. Embedding, sectioning and Hematoxylin & Eosin (HE) staining were performed by the UMass Medical School Morphology Core. Images were taken on a EVOS microscope.

Flow cytometry analysis of HSPCs and terminal erythroid differentiation

To assess HSPC populations, 10^6 cells were stained with the following antibodies: anti-CD4- BV605, anti-CD8a-BV-605, anti-Ter119-BV605, anti-CD45R-BV605, anti-Ly-6G/Ly-6C-BV605,

anti-C-kit-APC-eFluor 780, anti-Sca-1-BV711, anti-CD48-Alexa Fluor 700, anti-CD150-BV785, anti-CD34-PE, anti-CD16/32-Perycp-Cy5.5. BV-605$^-$cKit$^+$Sca$^+$cells were defined as LSK. BV-605$^-$ cKit$^+$Sca$^-$ cells were defined as LK. CD150$^+$CD48$^-$LSK cells were defined as LT-HSCs. CD150$^-$ CD48$^+$LSK cells were defined as ST-HSCs. CD150$^-$CD48$^-$LSK cells were defined as MPPs. CD34$^-$ CD16/32$^-$LK cells were defined as MEP. CD34$^+$CD16/32$^-$LK cells were defined as CMP. CD34$^+$CD16/32$^+$LK cells were defined as GMP. DAPI stain was used to exclude non-viable cells from analysis.

To assess erythropoiesis in the fetal liver, 5×10^5 cells were stained with the following antibodies: anti-Ter119-BV605, anti-CD71-PE, anti-CD45-APC-cy7, anti-CD220-APC-cy7 and anti-Ly6G/C- APC-cy7. APC-cy7$^-$ cells were used to analyze the expression of CD71 and Ter119. There are 6 stages were defined based on the expression of CD71 and Ter119 including CD71$^-$Ter119$^-$ (S0), CD71^{high}Ter119$^-$ (S1), CD71^{high}Ter119^{low} (S2), CD71^{high}Ter119^{high}(S3), CD71^{low}Ter119^{high} (S4), and CD71$^-$Ter119^{high} (S5). DAPI stain was used to exclude non-viable cells from analysis.

To assess erythropoiesis in the bone marrow and the spleen, 5×10^5 cells were stained with the following antibodies: anti-Ter119-BV605, anti-CD44-APC, anti-CD45-APC-cy7, anti-CD220-APC- cy7 and anti-Ly6G/C-APC-cy7. APC-cy7$^-$ cells were used to analyze proerythroblasts (ProEB) based on the expression of CD44$^+$ and Ter119$^-$. APC-cy7$^-$ cells were used to analyze BasoEB, PolyEB and OrthoEB based on the expression of CD44 and FSC. Flow cytometric analyses were performed on a LSRFortessa cytometer (BD Biosciences).

Colony formation assays

Methylcellulose colony formation assays were performed using Methocult M3334 (STEMCELL Tech), Methocult SF M3436 (STEMCELL Tech), Methocult SF M3434 (STEMCELL Tech), respectively. 20,000 cells from each fetal liver were used for colony formation assays. After 2 days, CFU-E colonies were scored blindly.

Western blot analysis

Fetal liver-derived cells were washed with cold PBS and lysed in 1X RIPA buffer (Thermo Scientific) supplemented with protease inhibitor cocktail (Sigma-Aldrich), phosphatase inhibitor cocktail III (Research Products International), and then centrifuged at 4 °C at 17,000 g for 15 min after incubating on ice for 15 min. Supernatant was diluted 1:1 with 2X Laemmli sample buffer (BioRad) under reducing conditions and boiled for 5 min at 100 °C. Samples with the same number of cells were separated via sodium dodecyl sulfate polyacrylamide gel electrophoresis (SDS-PAGE) and transferred to PVDF membranes. Membranes were blocked with 5% (wt/vol) milk in 1x Tris-Buffered Saline and 0.1% (vol/vol) Tween20 unless specified otherwise by antibody manufacturer. Primary antibodies were incubated overnight at 4 °C. Membranes were washed and incubated with horseradish peroxidase (HRP)-conjugated secondary antibodies for 1 h at room temperature (RT). Bands were detected using enhanced chemiluminescence (ECL) (Thermo Scientific). Quantifications of images were obtained using ImageJ software (NIH).

Polysome profiling assays

Freshly isolated fetal liver-derived c-Kit$^+$ cells and Ter119$^+$ cells were treated with emetine at 25 µg/ml for 15 min in IMDM medium at 37 °C before harvesting. Cells were washed with ice- cold PBS and then lysed with 300 µl of cold lysis solution containing 10 mM Tris ·HCl (pH 7.5), 100 mM KCl, 5 mM MgCl2, 1% Triton-100, 2 mM DTT, protease inhibitor (complete, EDTA-free, Roche), and RNase inhibitor (RNase OUT 1U/µl) and incubated on ice for 10 min, followed by centrifugation at 1300xg for 10 min at 4 °C. Cell lysates were then applied to the top of 10–50% sucrose gradients and subjected to ultracentrifugation in a Beckman SW41Ti rotor at 41,000 rpm for 2 h at 4 °C. A piston gradient fractionator (BioComp) and a 254 nm UV monitor with Data Quest Software were used to generate whole cell lysate polysome profiles.

Protein synthesis measurements

Fetal liver-derived cells were treated with opropargyl puromycin (OPP) in IMDM medium at 10 µM for 5 min before harvesting. Cells were washed once with cold PBS and then stained with antibodies

measuring HSCs for 30 min at RT. Cells were washed once (2% FBS in PBS) and fixed with 1% paraformaldehyde (PFA) in PBS for 15 min at 4 °C. Cells were washed once (2% FBS in PBS) and incubated in permeabilization buffer (3% FBS, 0.1% saponin in PBS) for 5 min at RT. Click chemistry mix was prepared following the instruction of Click-iT™ Edu Flow Cytometry Assay Kit (Invitrogen, C10632). Cells were incubated in Click chemistry mix at RT for 30 min and then washed twice with permeabilization buffer and twice with FACS buffer before flow cytometry analysis. Data were processed in FlowJo (BD) with a strategy to gate the different HSPC populations as described in the results. Mean fluorescent intensity (MFI) based on the click reaction (azide-fluor 488) for the gated populations was calculated for each sample.

Cell proliferation assay based on Edu incorporation

Fetal liver-derived cells were incubated with EdU at 10 mM for 25 min in IMDM medium at 37 °C before harvesting. Cells were washed once with cold PBS and then stained with antibodies measuring HSCs for 30 min at RT. Cells were washed once (2% FBS in PBS) and fixed with 1% paraformaldehyde (PFA) in PBS for 15 min at 4 °C. Cells were washed once (2% FBS in PBS) and incubated in permeabilization buffer (3% FBS, 0.1% saponin in PBS) for 5 min at RT. Click chemistry mix was prepared following the instruction of Click-iT™ Edu Flow Cytometry Assay Kit (Invitrogen, C10632). Cells were incubated in Click chemistry mix at RT for 30 min and then washed twice with permeabilization buffer and twice with FACS buffer before flow cytometry analysis. Data were processed in FlowJo (BD) with a strategy to gate HSC population. Mean fluorescent intensity (MFI) based on the click reaction (azide-fluor 488) for the gated populations was calculated for each sample.

Annexin V staining

Fetal liver-derived cells at indicated days were stained with the antibody panel of HSC, FITC- Annexin V (BioLegend) and DAPI as per manufacturers protocol. Cells were washed twice with FACS buffer before flow cytometry analysis. Data were processed in FlowJo (BD) with a strategy to gate HSC population. Annexin V^+ frequency for the gated populations was calculated for each sample.

Ferrous Iron measurements

Intracellular ferrous iron was measured by labeling cells with 5 µM BioTracker Far-red Labile Fe^{2+} Dye (Millipore Sigma) for 90 mins in PBS at 37 °C and analyzed by flow cytometry on a LSRFortessa cytometer (BD Biosciences).

CellROX measurements

Cells were stained in IMDM media at a final concentration of 5 µM for 30 mins at 37 °C. Cells were then spun down and washed with ice cold PBS three times and resuspended in the FACS buffer (PBS + 3% FBS) before analysis by flow cytometry on a LSRFortessa cytometer (BD Biosciences).

Lipid peroxidation measurements

Cells were stained with BODIPY C11 lipid probe (Invitrogen) according to the manufacturer's instructions. Briefly, the cells were stained by 5 µM of BODIPY 581/591 C11 reagent in PBS at 37 °C for 30 mins. Labeled cells were washed and analyzed on a LSRFortessa cytometer (BD Biosciences) with FITC and PE channels. Lipid peroxidation was calculated based on the ratio of MFI of FITC channel to MFI of PE channel.

RNA-seq pre-processing

Raw sequencing reads were aligned on the murine genome (mm10) using STAR (v2.7.8a), with the annotation of known genes from gencode vM35. Gene expression levels were then quantified using Salmon (1.4.0) and the annotation of protein coding genes from gencode v37.

Differential expression analyses & selection of dysregulated Candidate genes

Differential expression analyses were conducted on wild type, $Rps19^{lox/+}$ and $Rpl5^{lox/+}$ c-kit^+, and wt, $Rps19^{lox/+}$ and $Rpl5^{Lox/+}$ Ter119+ (referred as "condition") using DESeq2 (v1.48.1), with independent processing of the polysome-associated (POLY, translation) and cytoplasmic (CYTO, transcription) RNA groups. Genes lacking adjusted p-values due to low coverage were excluded, and log2 fold changes were corrected using the APEGLM shrinkage method (apeglm v1.30.0). A significance threshold (adjusted $p < 0.05$) and a log2FC cutoff = 1 were applied to both CYTO and POLY groups. Genes were categorized based on significance and direction of expression changes, distinguishing shared (BOTH_DOWN/UP) or group-specific (CYTO_DOWN/UP or POLY_DOWN/UP) regulations.

To better identify genes with non-parallel expression changes between CYTO and POLY, we applied a filtering approach. Genes significantly associated with one "condition" in at least one "group" were retained. Finally, a t-test ($p < 0.05$) assessed the significance of differences in expression changes between POLY and CYTO. Genes were classified as TRANSLA when changes were driven mainly by translation, BUFFER when transcriptional changes were buffered by translation, and STAB when variations of transcription and translation were correlated to a same extent. All these analyses were performed in R v4.5.0.

Gene Set Enrichement Analysis (GSEA) and single sample Gene Set Enrichement Analysis (ssGSEA)

GSEA was performed on POLY groups for each "condition" comparison, and significant pathways (among Hallmarks, M2, M5, M8 pathways available on MSigDB) were selected with a False Discovery Rate (FDR) threshold <0.05. ssGSEA was performed on all pathways of interest defined with GSEA in POLY groups. The score for each pathway of interest was computed with an adjusted p value < 0.05.

Bioinformatics support

RNA-seq quality controls and pre-processing were handled on the Gilles Thomas Bioinformatics platform (CRCL-CLB). RNA-seq Analyses were conducted collaboratively between the Gilles Thomas Bioinformatics Platform and the RibosOMICS Platform (CRCL).

Analysis of single-cell RNA sequence (scRNA)

For scRNA-seq experiments, freshly fetal liver-derived cells at E13.5 were washed with PBS containing 0.04% ultrapure BSA and resuspended in 0.04% ultrapure BSA in PBS on ice.10 K feta liver-derived single cells were used. Library construction was performed with Chromium Next GEM Single Cell 3' Library, Gel Bead & Multiplex Kit, and Chip Kit (10x Genomics) according to the manufacturer's instructions. 3' single-cell RNA-seq libraries generated with the 10x Genomics platform were processed using 10x Genomics Cell Ranger Suite (V7.0.0) with --include-introns option, which aligned the data to mm10 reference genome, de-multiplexing and generate UMI count matrix files. Downstream analyses were performed in R(V4.0.5) using Seurat (V.4.3.1). Seurat objects were created using filtered_feature_bc_matrix files. The percentage of mitochondrial reads were calculated for filtering the low-quality cells. High quality cells were selected for downstream analysis based on the following criteria: nFeature_RNA between 200 and 6,000, and percent.mt less than 5%. Each sample was normalized, and variable features were identified before integration and correcting batch effects. To identify anchor points for data integration, FindIntegrationAnchors function in

Seurat were used and finally, IntegrateData function were applied to obtain integrated Seurat object. Furthermore, Seurat standard pipeline(https://satijalab.org/seurat/archive/v4.3/integration_introduction) were used for downstream analysis: such as scale data, Principal Component Analysis, Uniform Manifold Approximation and Projection, and find clusters on integrated data. FindMarkers function was used to find the differential genes analysis with a minimum percentage of cells expressing the gene 5% and an average log fold-change threshold of 0.001. Gene set enrichment analysis was performed in python (V3.10.9) using gseapy (V1.1.4) package, a custom script is available at GitHub (https://github.com/gulkhan007/GSEA_scRNA).

Analysis of single cell multiome ATAC + GENE expression data

For single cell Multiome ATAC+Gene expression experiments, 10 K nuclei were isolated from fetal liver-derived cells at E13.5. Library construction was performed with Chromium Next GEM Single Cell Multiome ATAC+Gene expression reagent bundle, Gel Bead & Multiplex Kit, and Chip Kit (10x Genomics) according to the manufacturer's instructions. 10x Genomics Cell Ranger ARC pipeline (V2.0.0) was used to process the Single Cell Mutliome ATAC+Gene Expression libraries. Key steps involve barcode correction, alignment to mm10 reference genome, identification of accessible chromatin peaks, and generation of count matrix for both RNA and ATAC modalities. Furthermore, Seurat (V4.3.0) in R (V4.3.3) were utilized to create Seurat Objects from filtered RNA matrix files created by cellranger-arc. *CreateChromatinAssay* function in Seurat was used to add the ATAC data to the Seurat object. A shared peak file was created by merging peak files of each sample for integrated downstream analysis of ATAC data. Signac (V1.13.0) were used to calculate the Nucleosome Signal and Transcription start site enrichment of ATAC data. Quality of cells were obtained for further analysis by using the following criteria: nucleosome signal score <1.8, ATAC counts between 1800 and 35000, transcription start site enrichment score >1, and total RNA counts between 1000 and 25000. Before integration and removing of batch effects, RNA data was normalized, 2000 variable features were identified, data was scaled, and Principal Component Analysis was performed in Seurat. Harmony (V1.2.0) integration was used to integrate and remove the batch effects. Standard workflow (https://stuartlab.org/signac/articles/pbmc_multiomic) were used to process the ATAC data. FindMultiModalNeighbors function in Seurat were used to calculate joint neighbor graph, which represents both RNA expression and ATAC signal for further joint analysis of UMAP, and clustering. Findmarker function was used to find the differential genes and differentially accessible chromatin regions.

Statistical analysis

Unless otherwise indicated in the figure legends, all data are presented as mean ± standard deviation, using GraphPad Prism (v10.4.2). Student t-test (two-sided) or Wilcoxon rank test were used when two groups were compared, with Holm-Šídák correction when multiple comparisons were performed. When three or more groups were compared, we used one-way ANOVA, with Tukey's, Bonferroni's, or Dunnett's correction when multiple comparisons were performed. For survival comparisons, we used the Mantel-Cox log rank test.

All measurements were taken from distinct samples, with a minimum of 3 biological replicates. No statistical method was used to predetermine sample size. These were based on our previous experience and published literature on similar models to ensure the robustness of the observed phenotypes.

Resource Availability

Materials availability. All unique materials will be available upon request to the lead contact.

Reporting summary

Further information on research design is available in the Nature Portfolio Reporting Summary linked to this article.

Data availability

All sequencing datasets have been deposited to NCBI Gene Expression Omnibus under accession codes GSE304205 and GSE302344. Source data for plots can be found in the Source Data file. Any additional information with regards to the datasets is available from the lead contact upon request. Source data are provided with this paper.

References

1. Kovalski, J. R., Kuzuoglu-Ozturk, D. & Ruggero, D. Protein synthesis control in cancer: selectivity and therapeutic targeting. *EMBO J.* **41**, e109823 (2022).
2. Mazumder, B., Li, X. & Barik, S. Translation control: a multifaceted regulator of inflammatory response. *J. Immunol.* **184**, 3311–3319 (2010).
3. Storkebaum, E., Rosenblum, K. & Sonenberg, N. Messenger RNA translation defects in neurodegenerative diseases. *N. Engl. J. Med* **388**, 1015–1030 (2023).
4. Narla, A. & Ebert, B. L. Ribosomopathies: human disorders of ribosome dysfunction. *Blood* **115**, 3196–3205 (2010).
5. Farley-Barnes, K. I., Ogawa, L. M. & Baserga, S. J. Ribosomopathies: old concepts, New Controversies. *Trends Genet* **35**, 754–767 (2019).
6. Kampen, K. R., Sulima, S. O., Vereecke, S. & De Keersmaecker, K. Hallmarks of ribosomopathies. *Nucleic Acids Res.* **48**, 1013–1028 (2020).
7. Da Costa, L. et al. Diamond-Blackfan anemia, the archetype of ribosomopathy: How distinct is it from the other constitutional ribosomopathies? *Blood Cells Mol. Dis.* **106**, 102838 (2024).
8. Taylor, A. M. et al. Calmodulin inhibitors improve erythropoiesis in Diamond-Blackfan anemia. *Sci. Transl. Med.* **12**, eabb5831 (2020).
9. Liu, Y. L. et al. Animal models of Diamond-Blackfan anemia: updates and challenges. *Haematologica* **108**, 1222–1231 (2023).
10. Raiser, D. M., Narla, A. & Ebert, B. L. The emerging importance of ribosomal dysfunction in the pathogenesis of hematologic disorders. *Leuk. Lymphoma* **55**, 491–500 (2014).
11. Devlin, E. E., Dacosta, L., Mohandas, N., Elliott, G. & Bodine, D. M. A transgenic mouse model demonstrates a dominant negative effect of a point mutation in the RPS19 gene associated with Diamond-Blackfan anemia. *Blood* **116**, 2826–2835 (2010).
12. Matsson, H. et al. Targeted disruption of the ribosomal protein S19 gene is lethal prior to implantation. *Mol. Cell Biol.* **24**, 4032–4037 (2004).
13. Jaako, P. et al. Mice with ribosomal protein S19 deficiency develop bone marrow failure and symptoms like patients with Diamond-Blackfan anemia. *Blood* **118**, 6087–6096 (2011).
14. Paulson, R. F., Shi, L. & Wu, D. C. Stress erythropoiesis: new signals and new stress progenitor cells. *Curr. Opin. Hematol.* **18**, 139–145 (2011).
15. Da Costa, L., Leblanc, T. & Mohandas, N. Diamond-Blackfan anemia. *Blood* **136**, 1262–1273 (2020).
16. Giri, N. et al. Clinical and laboratory evidence for a trilineage haematopoietic defect in patients with refractory Diamond-Blackfan anaemia. *Br. J. Haematol.* **108**, 167–175 (2000).
17. Iskander, D. et al. Impaired cellular and humoral immunity is a feature of Diamond-Blackfan anaemia; experience of 107 unselected cases in the United Kingdom. *Br. J. Haematol.* **186**, 321–326 (2019).
18. Georgiades, P. et al. VavCre transgenic mice: a tool for mutagenesis in hematopoietic and endothelial lineages. *Genesis* **34**, 251–256 (2002).

19. Siegemund, S., Shepherd, J., Xiao, C. & Sauer, K. hCD2-iCre and Vav-iCre mediated gene recombination patterns in murine hematopoietic cells. *PLoS One* **10**, e0124661 (2015).
20. Chen, L. et al. Dynamic changes in murine erythropoiesis from birth to adulthood: implications for the study of murine models of anemia. *Blood Adv.* **5**, 16–25 (2021).
21. Shearstone, J. R. et al. Global DNA demethylation during mouse erythropoiesis in vivo. *Science* **334**, 799–802 (2011).
22. Yokomizo, T. et al. Independent origins of fetal liver haematopoietic stem and progenitor cells. *Nature* **609**, 779–784 (2022).
23. Purton, L. E. Adult murine hematopoietic stem cells and progenitors: an update on their identities, functions, and assays. *Exp. Hematol.* **116**, 1–14 (2022).
24. Signer, R. A., Magee, J. A., Salic, A. & Morrison, S. J. Haematopoietic stem cells require a highly regulated protein synthesis rate. *Nature* **509**, 49–54 (2014).
25. Pyronnet, S., Dostie, J. & Sonenberg, N. Suppression of cap-dependent translation in mitosis. *Genes Dev.* **15**, 2083–2093 (2001).
26. Wek, R. C. et al. Role of eIF2alpha kinases in translational control and adaptation to cellular stress. *Cold Spring Harb Perspect Biol.* **10**, a032870 (2018).
27. Gonzalez-Menendez, P. et al. Arginine metabolism regulates human erythroid differentiation through hypusination of eIF5A. *Blood* https://doi.org/10.1182/blood.2022017584 (2023).
28. Gutierrez, E. et al. eIF5A promotes translation of polyproline motifs. *Mol. Cell* **51**, 35–45 (2013).
29. Park, M. H. & Wolff, E. C. Hypusine, a polyamine-derived amino acid critical for eukaryotic translation. *J. Biol. Chem.* **293**, 18710–18718 (2018).
30. Schuller, A. P., Wu, C. C., Dever, T. E., Buskirk, A. R. & Green, R. eIF5A functions globally in translation elongation and termination. *Mol. Cell* **66**, 194–205 (2017).
31. O'Brien, K. A. et al. Molecular convergence in ex vivo models of Diamond Blackfan anemia. *Blood* https://doi.org/10.1182/blood-2017-01-760462 (2017).
32. Seimetz, J., Arif, W., Bangru, S., Hernaez, M. & Kalsotra, A. Cell-type specific polysome profiling from mammalian tissues. *Methods* **155**, 131–139 (2019).
33. Korsunsky, I. et al. Fast, sensitive and accurate integration of single-cell data with Harmony. *Nat. Methods* **16**, 1289–1296 (2019).
34. Zheng, G. X. et al. Massively parallel digital transcriptional profiling of single cells. *Nat. Commun.* **8**, 14049 (2017).
35. Ceccacci, E. et al. A refined single cell landscape of haematopoiesis in the mouse foetal liver. *J. Dev. Biol.* **11**, 15 (2023).
36. Wang, X. et al. Comparative analysis of cell lineage differentiation during hepatogenesis in humans and mice at the single-cell transcriptome level. *Cell Res.* **30**, 1109–1126 (2020).
37. Buttner, M., Ostner, J., Muller, C. L., Theis, F. J. & Schubert, B. scCODA is a Bayesian model for compositional single-cell data analysis. *Nat. Commun.* **12**, 6876 (2021).
38. Liu, Y. & Karlsson, S. Perspectives of current understanding and therapeutics of Diamond-Blackfan anemia. *Leukemia* **38**, 1–9 (2024).
39. Dixon, S. J. & Olzmann, J. A. The cell biology of ferroptosis. *Nat. Rev. Mol. Cell Biol.* **25**, 424–442 (2024).
40. Zhao, J. et al. Human hematopoietic stem cell vulnerability to ferroptosis. *Cell* **186**, 732–747 e716 (2023).
41. Cai, X. et al. Runx1 deficiency decreases ribosome biogenesis and confers stress resistance to hematopoietic stem and progenitor cells. *Cell Stem Cell* **17**, 165–177 (2015).
42. Yu, H. & Signer, R. A. J. Proteostasis disruption in inherited bone marrow failure syndromes. *Blood* **146**, 304–317 (2025).
43. Zheng, R. et al. Cistrome Data Browser: expanded datasets and new tools for gene regulatory analysis. *Nucleic Acids Res.* **47**, D729–D735 (2019).
44. Layer, R. M. et al. GIGGLE: a search engine for large-scale integrated genome analysis. *Nat. Methods* **15**, 123–126 (2018).
45. Link, V. M. et al. Analysis of genetically diverse macrophages reveals local and domain-wide mechanisms that control transcription factor binding and function. *Cell* **173**, 1796–1809 e1717 (2018).
46. Mingay, M. et al. Vitamin C-induced epigenomic remodelling in IDH1 mutant acute myeloid leukaemia. *Leukemia* **32**, 11–20 (2018).
47. Iskander, D. et al. Single-cell profiling of human bone marrow progenitors reveals mechanisms of failing erythropoiesis in Diamond-Blackfan anemia. *Sci. Transl. Med.* **13**, eabf0113 (2021).
48. Ulirsch, J. C. et al. The genetic landscape of diamond-blackfan anemia. *Am. J. Hum. Genet* **103**, 930–947 (2018).
49. Collins, A. et al. Maternal inflammation regulates fetal emergency myelopoiesis. *Cell* **187**, 1402–1421 e1421 (2024).
50. Rio, S. et al. Regulation of globin-heme balance in Diamond-Blackfan anemia by HSP70/GATA1. *Blood* **133**, 1358–1370 (2019).
51. Khajuria, R. K. et al. Ribosome levels selectively regulate translation and lineage commitment in human hematopoiesis. *Cell* **173**, 90–103 e119 (2018).
52. Yang, Z. et al. Delayed globin synthesis leads to excess heme and the macrocytic anemia of Diamond Blackfan anemia and del(5q) myelodysplastic syndrome. *Sci. Transl. Med.* **8**, 338ra367 (2016).
53. Hom, J., Dulmovits, B. M., Mohandas, N. & Blanc, L. The erythroblastic island as an emerging paradigm in the anemia of inflammation. *Immunol. Res* **63**, 75–89 (2015).
54. Paulson, R. F., Hariharan, S. & Little, J. A. Stress erythropoiesis: definitions and models for its study. *Exp. Hematol.* **89**, 43–54 e42 (2020).
55. Paulson, R. F., Ruan, B., Hao, S. & Chen, Y. Stress erythropoiesis is a key inflammatory response. *Cells* **9**, 634 (2020).
56. Yamazaki, S. et al. A mouse model of adult-onset anaemia due to erythropoietin deficiency. *Nat. Commun.* **4**, 1950 (2013).
57. Xiang, J., Wu, D. C., Chen, Y. & Paulson, R. F. In vitro culture of stress erythroid progenitors identifies distinct progenitor populations and analogous human progenitors. *Blood* **125**, 1803–1812 (2015).
58. Gabut, M., Bourdelais, F. & Durand, S. Ribosome and translational control in stem cells. *Cells* **9**, 497 (2020).
59. Chua, B. A. & Signer, R. A. J. Hematopoietic stem cell regulation by the proteostasis network. *Curr. Opin. Hematol.* **27**, 254–263 (2020).
60. Tiu, G. C. et al. A p53-dependent translational program directs tissue-selective phenotypes in a model of ribosomopathies. *Dev. Cell* **56**, 2089–2102 e2011 (2021).
61. Vlachos, A. et al. Increased risk of colon cancer and osteogenic sarcoma in Diamond-Blackfan anemia. *Blood* **132**, 2205–2208 (2018).
62. Dameshek, W. Riddle: what do aplastic anemia, paroxysmal nocturnal hemoglobinuria (PNH) and "hypoplastic" leukemia have in common? *Blood* **30**, 251–254 (1967).

Acknowledgements

We thank Fleur Bourdelais, Allyson Moureaux, Emile Thomas and Virginie Marcel from the RibosOMICS Platform at the CRCL for their help with the polysome sequencing analyses, and Stephen Baghdiguian and Kevin J. Tracey for scientific discussions. This work was supported by NIH grants R35HL171168 to L.B., R01DK141059 to J.D.C., the DBA Foundation and DBA Canada to J.D.C. and L.B, INCa (institute national du cancer) funding INCa_18488 (to S.D.), the Pediatric Cancer Foundation to J.M.L. and L.B., and ALSAC/St. Jude to J.D.C. L.B. was the recipient of an Allied World St. Baldrick's Scholar Award.

Author contributions

Conceptualization: N.T., S.D., J.D.C., L.B.; investigation: Y.T., T.L, R.M., A.B., J.P., M.K., R.R.; formal analysis: Y.T., T.L., R.M., A.B., J.P., J.X., V.S., Ja.P., L.A.S., B.J.B., Y-R. Z., P.M., R.A.J.S., J.M.L., I.R., D.I., L.I.Z., S.B., M.J.W., P.G.G., N.M., N.T., S.D., J.D.C., L.B.; writing–original draft: L.B.;

writing–review & editing: Y.T., T.L., R.M., A.B., J.P., M.K., R.R, J.X., V.S., Ja.P., L.A.S., B.J.B., Y-R. Z., P.M., R.A.J.S., J.M.L., I.R., D.I., L.I.Z., S.B., M.J.W., P.G.G., N.M., N.T., S.D., J.D.C., L.B.; funding acquisition: J.D.C., L.B.; supervision: N.T., S.D., J.D.C, L.B.; project administration: J.D.C., L.B.

Competing interests
The authors declare no competing interests.

Additional information
Supplementary information The online version contains supplementary material available at https://doi.org/10.1038/s41467-026-71727-y.

Correspondence and requests for materials should be addressed to Lionel Blanc.

Peer review information *Nature Communications* thanks the anonymous reviewer(s) for their contribution to the peer review of this work. A peer review file is available.